An analytical model of the dynamic response of circular composite plates to high-velocity impact

A. Schiffer[a,b,*], W.J. Cantwell[a] and V.L. Tagarielli[b]

[a] *Khalifa University of Science, Technology and Research (KUSTAR), Abu Dhabi, UAE*

[b] *Department of Aeronautics, Imperial College London, SW7 2AZ, UK*

Abstract

Analytical models are developed to predict the transient elastic response of fully clamped circular composite plates subject to high-velocity impact by a rigid spherical projectile. The models are based on first-order shear deformation plate theory and account for the effects of large deformations as well as propagation and reflexion of flexural waves. Analytical predictions of plate deflection history and peak strain in the plates are found in good agreement with those obtained from detailed explicit FE simulations. The dynamic response is found to be governed by four non-dimensional parameters and two characteristic regimes of behaviour are identified. The models are used to construct maps to design impact-resistant composite plates.

Keywords: ballistic limit, finite element, wave propagation, plate theory, impact damage

Submitted to *International Journal of Impact Engineering*, January 2015

[*] Corresponding author, T: +971-(0)2-4018204, E: andreas.schiffer@kustar.ac.ae

1. Introduction

Fibre-reinforced composite materials are progressively employed as structural materials in light-weight ships, road vehicles, aircraft components and armour systems, due to their low weight, high stiffness and excellent corrosion resistance. The resistance of composite plates to high-velocity impact is a concern in many industrial applications. In the last decades, significant effort has been devoted to foster understanding of the dynamic response of composite laminates consequent to localised impact loading. In composite materials, energy absorbtion due to plastic deformation is very limitied and their response to localised transverse impact leads to deformation modes dictated by propagation of longitudinal, shear and flexural waves travelling in the material at different velocities [1].

The damage and failure modes of composites upon impact depend on the plate geometry, impact velocity as well as on the shape and mass of the projectile. The impact resistance of a structure is often quantified by the limit velocity (or ballistic limit), defined as the velocity required for a projectile to penetrate a given material at least 50% of the time. When laminates are impacted at velocities below the ballistic limit, matrix cracking and delamination have been recognised to be the main energy dissipation mechanisms. Takeda et al. [2] conducted impact tests on glass-fibre/epoxy laminates and used high-speed photography to observe the growth of delamination cracks propagating in the samples, concluding that delamination growth was associated with flexural wave propagation. Post-impact matrix cracks and delaminations were also observed by Heimbs et al. [3], who conducted an experimental and numerical study of the impact behaviour of CFRP composites subject to compressive and tensile preloads, concluding that tensile preloading leads to a reduction in delamination while compressive preloading facilitates delamination. At impact velocities near the ballistic limit, they also observed fibre failure in addition to delaminations and matrix cracks. Other authors [4, 5] employed theoretical modelling approaches to study delamination of laminates subject to transverse impact. Some authors have investigated the mechanism of plate spalling induced by reflection of through-thickness stress waves, see e.g. [6].

Studies investigating the deformation and failure mechanisms of laminates impacted above the ballistic limit are extensively described in the literature and a comprehensive review of existing work on this subject can be found in Abrate [7]. For example, Cantwell and Morton [8] observed the mechanisms of perforation of thin CFRP beams and noted that plate failure involved a shear-off penetration in the upper half of the plate (impact side) and tensile breakage of plies in the bottom half. The effect of projectile geometry on the perforation resistance of fibre-reinforced composites was investigated by Wen [9], who derived a simple empirical relationship for the ballistic limit by assuming that the resistance provided by the laminate is composed of a static and a dynamic term, with the latter dependending on the nose shape of the projectile. Mines et al. [10] conducted ballistic tests on woven, z-stitched and through-thickness reinforced glass/polyester laminates, varying laminate thickness as well as mass and geometry of the projectile. Their results showed only small differences in the impact behaviour of the different composite systems investigated.

While carbon-fibre (CFRP) and glass-fibre reinforced laminates (GFRP) are the most widely used material systems in engineering applications, the recent development of new fibres with extremely high stiffness to weight ratios has greatly improved the ballistic performance of fibre-composites. They include Nylon, aramids (e.g. Kevlar®), ultra-high molecular weight polyethylene (e.g. Spectra®, Dyneema®) and PBO (e.g. Zylon®). Zhu et al. [11] performed dynamic perforation tests on Kevlar/polyester laminates and found that they outperform aluminium plates of equal weight in terms of impact resistance. They also tested laminates with deliberately introduced delaminations and the results showed that the ballistic limit was not greatly affected by such defects.

In an attempt to relate the ballistic performance of a given laminate to the velocity and geometry of the projectile, Cunniff [12] proposed a set of non-dimensional parameters and argued that the ballistic limit of fibre composites scales with a characteristic velocity determined by the material properties of the fibres. However, for some types of laminate, the characteristic velocity introduced by Cunniff does not accurately capture the experimental data. For example, Karthikeyan et al. [13] recently measured the ballistic performance of Dyneema® plates (ultra-high molecular weight polyethylene fibre composite) and found that the characteristic velocity required to normalise the perforation data cannot be deduced from the fibre properties. Their observations showed that the propagation of flexural wave fronts followed an almost square-like pattern, due to the extremely low shear strength of this type of laminate, whereas those observed on CFRP plates were almost circular.

A considerable body of literature exists on numerical and theoretical predictions of the elastic response of composite plates subject to various dynamic loading conditions. A possible analytical treatment of impact on elastic plates follows that given in Zener [14] who expressed the transient response of thin simply-supported isotropic plates in terms of mode shapes and natural frequencies. A similar approach was used by Olsson [15] who extended the theory of Zener [14] to the case of orthotropic plates. Sun and Chattopadyay [16] employed a similar technique to investigate the central impact of a mass on a simply-supported laminated composite plate under initial stress by employing a plate theory that accounts for transverse shear deformations [17]. They also noted that rotary inertia has only a minor effect on the dynamic response. Dobyns [18] also used plate theory [17] to analyse the dynamic response of composite plates subject to loading by pressure pulses of various shapes, in order to mimic different types of blast loading. Finite strain solutions for the impact behaviour of elastic plates with fully-clamped boundaries are obtained in the published literature via approximate techniques, since closed-form solutions are not available in this case. For example, the Rayleigh-Ritz method was employed by Qian & Swanson [19] for the case of impacted rectangular carbon/epoxy plates. A reduced model for predicting the dynamic deformation modes is presented in Hoo Fatt and Palla [20] for the case of composite sandwich plates subject to loading by a prescribed pressure history. Phoenix and Porwal [21] derived a theoretical model for the 2D response of an initially unloaded elastic membrane impacted transversely by a cylindrical projectile, predicting that the structural response comprised propagation of tensile waves and ‚cone waves‘ emanating from the impact point, with the cone wave travelling at lower speed. The theory was used to predict the ballistic resistance of composite systems and predictions were found in agreement with Cunniff’s scaling theory [12].

In this study we derive an analytical model for the dynamic response of a fully-clamped, circular composite plate subject to high velocity impact by a rigid projectile. Effects of transverse shear deformations, large deflections and flexural wave propagation will be taken into account. In addition, the effect of higher order vibrational modes, activated upon reflection of flexural waves at the boundaries, will also be modelled. The model is based on a linear elastic material response but accounts for the geometric non-linearities in the problem and, to some extent, for material anisotropy.

It is clear that the prediction of the ballistic limit of arbitrary composite plates is beyond the scope of the present study, which does not attempt modelling the complex damage mechanisms activated in composite laminates upon impact. On the other hand the model presented here provides, for a certain class of composite plates and for an arbitrary projectile, the critical impact velocity at the onset of tensile ply failure; this information is readily used in the design of components exposed to a substantial threat of impact loading (e.g., impact of runway debris or similar on aircraft structures). The model allows identifying the four main governing non-dimensional groups of the impact problem and predicts two possible, distinctive regimes of behaviour.

The outline of this paper is as follows: in Sections 2 and 3 we derive the analytical models and describe the FE scheme employed; in Section 4 we validate the analytical models by comparing analytical and FE predictions; in Section 5 the validated analytical model is used to compare the damage resistance of glass-fibre and carbon-fibre reinforced composite plates, and non-dimensional design maps are constructed for both types of laminate.

2. Analytical modelling

The elastic response of composite plates to high-velocity impact by rigid projectiles is dictated by propagation of flexural waves, shear waves and extensional waves travelling in the material at different velocities. In fibre-reinforced composites, wave speeds are different when measured along different axes or directions due to the anisotropic behaviour of the material, see e.g. Sierakowski and Chaturvedi [22] for a comprehensive account of the dynamic behaviour of fibre-reinforced composites. Due to the complexity of the problem, exact solutions are restricted to the use of numerical methods which require high computational effort, especially when parametric studies are being conducted.

The objective of this study is to develop an approximate analytical model able to provide, in a computationally efficient way, reliable predictions of plate deformation associated with the dynamic elastic response a circular composite laminate subject to high-velocity impact. In this section, we employ an approach similar to that of Schiffer and Tagarielli [23] to derive the equations of motion in form of non-dimensional ODEs, and to identify the governing non-dimensional parameters; various assumptions concerning plate deformation and material behaviour will be explained and discussed in detail. Finally, we define two characteristic deformation regimes and construct a regime map.

2.1 Governing equations

2.1.1 Material modelling

In this study we consider symmetric composite laminates comprised of a stack of transversely isotropic plies with equally spaced fibres (quasi-isotropic layups such as $\left[0/\pm60^{\mathrm{o}}\right]_S$, $\left[0/45^{\mathrm{o}}/90^{\mathrm{o}}/-45^{\mathrm{o}}\right]_S$ and so forth. In a first approximation, we neglect the directionality of material stiffness in the circumferential direction of the plate (in case of a cross-ply laminate for example) and adopt the concept of effective (or average) laminate stiffness. In doing so, we define the four effective elastic constants

$$E_r = \frac{1}{hA'_{11}} \qquad \nu_{r\varphi} = -\frac{A'_{12}}{A'_{11}} \qquad E_{fr} = \frac{12}{h^3 D'_{11}} \qquad G_r = \frac{1}{hS'_{11}} \tag{1}$$

where E_r, $\nu_{r\varphi}$, E_{fr} and G_r are the effective in-plane modulus, Poisson's ratio, flexural modulus and transverse shear modulus, respectively, and A'_{11} is the first element of the laminate's compliance matrix, $\mathbf{A}' = \mathrm{inv}(\mathbf{A})$. It is important to mention that the stiffnesses A'_{11}, A'_{12}, D'_{11} and S'_{11} in eq. (1) are, in general, dependent on the choice of reference system and vary along the circumferential direction ϕ. In order to obtain effective averages, the properties were evaluated n times (typically $n = 8$) in different reference systems obtained by rotating an arbitrary cylindrical system about the z-axis by increments $\phi_j = 2\pi j / n$ ($j = 0,1,\ldots,n$) and the corresponding properties E_r^j, G_r^j and $\nu_{r\varphi}^j$ were averaged to obtain the effective laminate properties as

$$\tilde{E}_r = \frac{1}{n}\sum_{j=0}^{n} E_r^j \qquad \tilde{\nu}_{r\varphi} = \frac{1}{n}\sum_{j=0}^{n} \nu_{r\varphi}^j \qquad \tilde{G}_r = \frac{1}{n}\sum_{j=0}^{n} G_r^j . \tag{2}$$

The response of the composite is isotropic in the plane of the plate but has bending and shear moduli independent of the in-plane properties. For the composites modelled in this work, the very small differences between E_{fr} and E_r allowed to assume $\tilde{E}_{fr} \approx \tilde{E}_r$.

It should be mentioned here that the assumption of axisymmetric plate deformation is not ideal for all types of composites; for example experiments [13] have shown that impact on composite systems with very low shear strength (e.g. Dyneema®) results in flexural waves propagating outwards with square wave-fronts. The models developed in this paper are not adequate for this type of composites.

2.1.2 Problem geometry and modelling approach

Consider a fully clamped circular plate of thickness h and radius R made from a composite laminate (see Section 2.1.1) of areal mass $\mu = \rho h$, as sketched in Fig. 1 (ρ denotes the average density of the laminate). The plate is subject to dynamic transverse loading by impact of a rigid spherical projectile of mass M and radius R_s, travelling at a velocity v_0 perpendicular to the plate surface (Fig. 1a). Here, attention is restricted to impact of relatively large projectiles, i.e. $2R_s > h$, on plates with small to moderate aspect ratios, $0.02 < h/R < 0.15$. For these ranges it is reasonable to use the thin plate assumption which neglects local plate indentations.

As sketched in Fig. 1b, we assume that the initial phase of response is dictated by propagation of a flexural wave, emanating from the impact point and propagating towards the boundary. Despite the dispersive behaviour of flexural waves [1], impact experiments on composite plates [13, 24] have shown that the shape of the dynamic disturbance does not appreciably change during this phase and that the flexural wave front can be idealised by an elastic wave front propagating at a velocity $\dot{\zeta}$ in the positive *r*-direction, see Fig. 1b. In the light of these observations, we assume a simple axisymmetric polynomial displacement field to describe the initial deformation response of the composite plate, $w(r,t)$, in terms of two degrees of freedom: the centre deflection $w_0(t)$ and the flexural wave position $\zeta(t)$. When the flexural wave front reaches the boundary of the plate, i.e. $\zeta = R$ (see Fig. 1c), the plate deflection profile is affected by the boundary conditions. We denote as 'Phase 1' the response ranging from $t = 0$ to the instant when the flexural wave reaches the plate's centre point, t_1, i.e. $\zeta(t_1) = R$, while 'Phase 2' represents the response at subsequent times.

2.1.3 Phase 1 response: $0 \le t \le t_1$

We proceed to derive the governing equations for the plate's response during Phase 1. In plate theory, it is convenient to introduce stress resultants in terms of the forces and moments applied to the plate's middle surface (per unit length of laminate side) which are defined as

$$\begin{pmatrix} N_{rr} \\ N_{\varphi\varphi} \\ N_{r\varphi} \end{pmatrix} = \int_{-h/2}^{h/2} \begin{pmatrix} \sigma_{rr} \\ \sigma_{\varphi\varphi} \\ \sigma_{r\varphi} \end{pmatrix} dz \qquad \begin{pmatrix} M_{rr} \\ M_{\varphi\varphi} \\ M_{r\varphi} \end{pmatrix} = \int_{-h/2}^{h/2} \begin{pmatrix} \sigma_{rr} \\ \sigma_{\varphi\varphi} \\ \sigma_{r\varphi} \end{pmatrix} zdz \qquad \begin{pmatrix} Q_{r} \\ Q_{\varphi} \end{pmatrix} = \int_{-h/2}^{h/2} \begin{pmatrix} \tau_{rz} \\ \tau_{\varphi z} \end{pmatrix} dz \tag{3}$$

where N_i, M_i and Q_i are the in-plane forces, bending/twisting moments and transverse shear forces, respectively.

Here, we employ the first-order shear deformation theory of plates (i.e. Mindlin plate theory) based on the von Karman strain relations, which account for non-linear terms in the in-plane strain response due to stretching of the plate's mid-surface. Note that for transverse loading cases, it is widely accepted that the radial and tangential mid-plane displacements are vanishingly small compared to the transverse deflections; then, the kinematic relations are

$$u(r,z,t) = z\theta_r(r,t) \qquad w(r,z,t) = w(r,t) \tag{4}$$

where *u* and *w* are the displacements in the *r* and *z* directions, respectively, and θ_r denotes the rotation of the cross-section in the *rz*-plane, with reference to the coordinate system shown in Fig. 1. Employing eq. (4) and imposing axisymmetric deformations, the von Karman strain-displacement relations can be written as

$$\varepsilon_{rr} = \frac{1}{2}\left(\frac{\partial w(r,t)}{\partial r}\right)^2 + z\frac{\partial \theta_r(r,t)}{\partial r} \qquad \varepsilon_{\varphi\varphi} = \varepsilon_{r\varphi} = \gamma_{r\varphi} = 0 \qquad \gamma_{rz} = \frac{\partial w(r,t)}{\partial r} + \theta_r(r,t) \tag{5}$$

and the corresponding curvatures of the middle-surface with respect to the angle of rotation, $\theta_r(r,t)$, are

$$\kappa_{rr} = \frac{\partial \theta_r}{\partial r} \qquad \kappa_{\varphi\varphi} = \frac{1}{r}\theta_r \qquad \kappa_{r\varphi} = 0. \tag{6}$$

Let us now assume that plate deformation within the portion $0 \le r \le \zeta(t)$ can be approximated by an axisymmetric polynomial shape function that satisfies the boundary conditions of the problem. Such a function may be written as

$$w(r,t) = w_0(t)\left[1 - \frac{3r^2}{\zeta(t)^2} + \frac{2r^3}{\zeta(t)^3}\right] \tag{7}$$

where $w_0(t)$ denotes the plate's centre deflection and $\zeta(t)$ is the flexural wave position (Fig. 1b); for $r > \zeta(t)$, the plate is assumed to remain straight during Phase 1, hence $w(r,t) = 0$. A shear deformation profile that is compatible with the boundary conditions and symmetry requirements is given by

$$\gamma_{\mathrm{rz}}(r,t) = \gamma_{\mathrm{rz0}}(t)\sin\left(\frac{r\pi}{\zeta(t)}\right)^2 \tag{8}$$

with $\gamma_{\mathrm{rz0}}(t)$ the shear deformation amplitude.

The constitutive description for the composite laminate is treated as follows. For a symmetric laminate, the relationship between the in-plane forces N_i and the corresponding strains ε_i is

$$\begin{pmatrix} N_{rr} & N_{\varphi\varphi} & N_{r\varphi} \end{pmatrix}^{\mathrm{T}} = \mathbf{A}\cdot\begin{pmatrix} \varepsilon_{rr} & \varepsilon_{\varphi\varphi} & \gamma_{r\varphi} \end{pmatrix}^{\mathrm{T}} \tag{9}$$

where $\mathbf{A}$ denotes the in-plane stiffness matrix of the laminate. Similarly, the bending and twisting moments M_i can be related to the corresponding curvatures κ_i as

$$\begin{pmatrix} M_{rr} & M_{\varphi\varphi} & M_{r\varphi} \end{pmatrix}^{\mathrm{T}} = \mathbf{D}\cdot\begin{pmatrix} \kappa_{rr} & \kappa_{\varphi\varphi} & \kappa_{r\varphi} \end{pmatrix}^{\mathrm{T}} \tag{10}$$

with $\mathbf{D}$ the bending stiffness matrix of the laminate, and for transverse shear deformations the stress-strain relationship is given by

$$\begin{pmatrix} Q_{\mathrm{rz}} & Q_{\varphi\mathrm{z}} \end{pmatrix}^{\mathrm{T}} = k\,\mathbf{S}\cdot\begin{pmatrix} \gamma_{\mathrm{rz}} & \gamma_{\varphi\mathrm{z}} \end{pmatrix}^{\mathrm{T}} \tag{11}$$

where $\mathbf{S}$ is the shear stiffness matrix of the laminate and the constant k denotes the shear correction factor; note that in Mindlin's plate theory, $k = 5/6$ for rectangular cross-sections.

Employing first-order shear theory of plates, the constitutive equations are

$$\begin{array}{lll} N_{rr} = C\left(\varepsilon_{rr} + \tilde{\nu}_{r\varphi}\varepsilon_{\varphi\varphi}\right) & N_{\varphi\varphi} = C\tilde{\nu}_{r\varphi}\varepsilon_{rr} & N_{r\varphi} = 0\ ; \\ M_{rr} = -D\left(\kappa_{rr} + \tilde{\nu}_{r\varphi}\kappa_{\varphi\varphi}\right) & M_{\varphi\varphi} = -D\left(\kappa_{\varphi\varphi} + \tilde{\nu}_{r\varphi}\kappa_{rr}\right) & M_{r\varphi} = 0\ ; \\ Q_{rz} = k\tilde{G}_r h\gamma_{rz} & Q_{\varphi z} = 0\ . & \end{array} \tag{12}$$

after defining the axial rigidity C as

$$C = \frac{\tilde{E}_r h}{1-\tilde{\nu}_{r\varphi}{}^2} \tag{13}$$

and the bending rigidity D as

$$D = \frac{\tilde{E}_r h^3}{12\left(1-\tilde{\nu}_{r\varphi}{}^2\right)}. \tag{14}$$

Now write the total elastic energy of the plate as the sum of the strain energies associated to bending, membrane and transverse shear

$$U = U_b + U_m + U_s = \\ = \frac{1}{2} 2\pi \int_0^{\zeta(t)} \left(M_{rr}\kappa_{rr} + M_{\varphi\varphi}\kappa_{\varphi\varphi} \right) r dr + \frac{1}{2} 2\pi \int_0^{R} \left(N_{rr}\varepsilon_{rr} + N_{\varphi\varphi}\varepsilon_{\varphi\varphi} \right) r dr + \frac{1}{2} 2\pi \int_0^{\zeta(t)} Q_{rz}\gamma_{rz} r dr. \tag{15}$$

Substituting eqs. (5), (6), (7), (8) and (12) in eq. (15) and evaluating the integral terms gives

$$U = \frac{\pi D}{8\zeta^2}\left[26.38\gamma_{\mathrm{rz0}}^2\zeta^2 + 72 w_0 \left(\gamma_{\mathrm{rz0}}\zeta + w_0 \right) \right] + \frac{\pi \tilde{E}_r h}{8\left(1-\tilde{\nu}_{r\varphi}^2\right)} \frac{w_0^4}{\zeta^2} + \frac{5\pi \tilde{G}_r h}{32} \gamma_{\mathrm{rz0}}^2 \zeta^2 \tag{16}$$

The derivation of the membrane energy, represented by the second term of eq. (16), merits some further comment. The nonlinear term in ε_{rr}, as defined in eq. (5), provides the relationship between the transverse displacement w_0 and the membrane strain in the radial direction, and predicts zero strain within the straight portion of the plate, $r > \zeta(t)$. However, this contradicts experimental observations [25] and theoretical models [21] which suggest that a tensile precursor wave emanates from the impact point and propagates radially towards the plate boundary, at a velocity higher than that of the flexural wave speed, thus inducing tensile radial stresses in the portion $r > \zeta(t)$. The presence of such precursor waves have also been detected in our FE calculations, as detailed in Section 3. For the range of geometries considered here (see Section 2.1.2), preliminary FE simulations have shown that the propagation velocity of the tensile precursor wave is much higher than that of the flexural wave and it is therefore reasonable to neglect the propagation of the precursor wave and to assume that the membrane strain, ε_{rr}^m, is uniform in the radial direction and approximately equal to the average strain induced in an ideal membrane with a vanishing curvature, $\kappa_{rr} = 0$. Hence, we write

$$\varepsilon_{rr}^m = \frac{1}{2}\frac{w_0^2}{R\zeta}. \tag{17}$$

Previous studies [16] have shown that the effects of rotary inertia play only a minor role in the impact response of composite plates and are therefore neglected in our analysis. Then the total kinetic energy of the system is given by

$$T = \frac{1}{2} 2\pi\mu \int_0^{\zeta(t)} \left(\frac{\partial w}{\partial t} \right)^2 r dr + \frac{1}{2} M \left(\frac{\partial w_0}{\partial t} \right)^2 = \\ = \pi\mu \left(0.214 w_0^2 \dot{\zeta}^2 + 0.171 w_0 \dot{w}_0 \zeta \dot{\zeta} + 0.0857 \dot{w}_0^2 \zeta^2 \right) + \frac{1}{2} M \dot{w}_0^2 . \tag{18}$$

Here, the over-dots denote derivatives with respect to time.

The Euler-Lagrange equations are now employed to solve for the time history of the degrees of freedom $w_0(t)$, $\zeta(t)$ and $\gamma_{\mathrm{rz}0}(t)$. The Lagrangian function

$$L = T - U \tag{19}$$

is obtained by combining eqs. (16) and (18), and is used to derive the equations of motion of the system via the Euler-Lagrange equations

$$\frac{\mathrm{d}}{\mathrm{d}t}\left(\frac{\partial L}{\partial \dot{w}_0}\right) - \frac{\partial L}{\partial w_0} = 0 \qquad \frac{\mathrm{d}}{\mathrm{d}t}\left(\frac{\partial L}{\partial \dot{\zeta}}\right) - \frac{\partial L}{\partial \zeta} = 0 \qquad \frac{\mathrm{d}}{\mathrm{d}t}\left(\frac{\partial L}{\partial \dot{\gamma}_{\mathrm{rz}0}}\right) - \frac{\partial L}{\partial \gamma_{\mathrm{rz}0}} = 0. \tag{20}$$

Evaluating the derivatives in eq. (20) and writing the equations of motion in non-dimensional terms, we find that the non-dimensional generalised coordinates

$$\bar{w}_0 = \frac{w_0}{R} \qquad \bar{\zeta} = \frac{\zeta}{R} \qquad \gamma_{\mathrm{rz}0} \tag{21}$$

are functions of the non-dimensional time $\bar{t} = t\sqrt{E/\rho}/R$ and of the following set of non-dimensional parameters

$$\bar{h} = \frac{h}{R} \qquad \bar{M} = \frac{M}{\rho h R^2 \pi} \qquad \bar{v}_0 = v_0\sqrt{\frac{\rho}{\tilde{E}_r}} \qquad \bar{G} = \frac{\tilde{G}_r}{\tilde{E}_r}\ . \tag{22}$$

Here, $\bar{w}_0$ and $\bar{\zeta}$ represent the normalised centre deflection and flexural wave position, respectively, while the parameters $\bar{h}$, $\bar{M}$ and $\bar{v}_0$ denote aspect ratio, mass ratio and non-dimensional impact velocity, respectively.

After some algebraic manipulation the non-dimensional governing equations for the Phase 1 response of the plate are obtained as

$$\begin{aligned}&0.318\left(0.171\bar{w}_0\dot{\bar{\zeta}}^2 + 0.171\bar{w}_0\bar{\zeta}\ddot{\bar{\zeta}} + 0.514\dot{\bar{w}}_0\bar{\zeta}\dot{\bar{\zeta}} + 0.171\ddot{\bar{w}}_0\bar{\zeta}^2 + \bar{M}\ddot{\bar{w}}_0\right) = \\ &= \frac{0.159}{\bar{\zeta}^2\left(1-\tilde{\nu}_{r\varphi}^2\right)}\left[0.857\bar{w}_0\bar{\zeta}^2\dot{\bar{\zeta}}^2\left(1-\tilde{\nu}_{r\varphi}^2\right) + 3\bar{h}^2\left(\frac{\gamma_{\mathrm{rz}0}\bar{\zeta}}{2} + \bar{w}_0\right) + \bar{w}_0^{\,3}\right]\end{aligned} \tag{23}$$

$$\begin{aligned}&4\left[0.1071\bar{w}_0^2\bar{\zeta}\ddot{\bar{\zeta}} + 0.257\bar{w}_0\dot{\bar{w}}_0\bar{\zeta}\dot{\bar{\zeta}} + 0.0428\bar{\zeta}^2\left(\bar{w}_0\ddot{\bar{w}}_0 + \dot{\bar{w}}_0^2\right)\right] = \\ &= \frac{1}{2\bar{\zeta}^2\left(1-\tilde{\nu}_{r\varphi}^2\right)}\left[0.343\dot{\bar{w}}_0^2\bar{\zeta}^4\left(1-\tilde{\nu}_{r\varphi}^2\right) - \frac{5\bar{G}}{8}\gamma_{\mathrm{rz}0}^2\bar{\zeta}^4\left(1-\tilde{\nu}_{r\varphi}^2\right) + 3\bar{h}^2\left(\frac{\gamma_{\mathrm{rz}0}\bar{w}_0\bar{\zeta}}{2} + \bar{w}_0^2\right) + \frac{\bar{w}_0^{\,2}}{2}\right]\end{aligned} \tag{24}$$

$$0 = \bar{h}^2\left(0.549\gamma_{\mathrm{rz}0}\bar{\zeta} + 0.75\bar{w}_0\right) + 0.3125\bar{G}\gamma_{\mathrm{rz}0}^2\bar{\zeta}^3\left(1-\tilde{\nu}_{r\varphi}^2\right). \tag{25}$$

The impact event can be mathematically described by the following initial conditions

$$\bar{w}_0\left(\bar{t}=0\right) = 0 \qquad \dot{\bar{w}}_0\left(\bar{t}=0\right) = \bar{v}_0 \qquad \bar{\zeta}\left(\bar{t}=0\right) = 0 \qquad \dot{\bar{\zeta}}\left(\bar{t}=0\right) = 0 \tag{26}$$

where $\overline{v}_0 = v_0\sqrt{\rho / \tilde{E}_r}$ is the non-dimensional impact velocity. The initial value problem can be numerically integrated to obtain the histories $\overline{w}_0\left(\overline{t}\right)$, $\overline{\zeta}\left(\overline{t}\right)$ and $\gamma_{\mathrm{rz0}}\left(\overline{t}\right)$.

It can be seen from eqs. (16) and (18) that the Lagrangian function (19) is independent of the plate radius R and therefore the Phase 1 solutions are unaffected by the boundary conditions, as for the case of a plate with infinite radius. The Phase 1 solutions cease being valid when the flexural wave reaches the plate boundary, $\overline{\zeta}\left(\overline{t}_1\right)=1$, as different deformation modes are induced by the interaction with the plate's supports. Correspondingly we modify the shape functions for Phase 2 response, as detailed in the following section.

2.1.4 Phase 2 response: $t > t_1$

We proceed to derive the governing equations for the ensuing Phase 2 response. The reflection of flexural waves at the clamped plate boundary, commencing at $t = t_1$, gives rise to transverse oscillations at higher frequencies which affect the response of the plate. Such phenomena are not addressed in the current literature [14, 15, 21]; here we construct an approximate model able to predict the effects of the supports upon the dynamic response of the laminates. In order to obtain a tractable system of governing equations for the Phase 2 response, only a limited number of mode shapes can be considered. In a first approximation, we add two sinusoidal shape functions to the polynomial shape function considered for Phase 1, as

$$w\left(r,t\right) = w_0\left(t\right)\left[1-\frac{3r^2}{R^2}+\frac{2r^3}{R^3}\right]+w_1\left(t\right)\sin\left(\frac{r\pi}{R}\right)^2+w_2\left(t\right)\cos\left(\frac{3r\pi}{2R}\right)^2 \tag{27}$$

where $w_1\left(t\right)$ and $w_2\left(t\right)$ are the vertical displacement amplitudes corresponding to the first and second sinusoidal terms, respectively. It should be mentioned that only the first and last terms in eq. (27) contribute to the centre deflection, $w\left(r=0,t\right)$, therefore

$$w_{\mathrm{tot}}\left(t\right) = w_0\left(t\right)+w_2\left(t\right) \tag{28}$$

is the total centre deflection in Phase 2. Accordingly, the shear deflections in Phase 2 are modified to

$$\gamma_{\mathrm{rz}}\left(r,t\right) = \gamma_{\mathrm{rz0}}\left(t\right)\sin\left(\frac{r\pi}{R}\right)^2+\frac{\gamma_{\mathrm{rz1}}\left(t\right)}{2}\sin\left(\frac{2r\pi}{R}\right)+\frac{\gamma_{\mathrm{rz2}}\left(t\right)}{2}\sin\left(\frac{3r\pi}{R}\right) \tag{29}$$

where $\gamma_{\mathrm{rz1}}(t)$ and $\gamma_{\mathrm{rz2}}(t)$ are the shear deformation amplitudes associated to the first and second sinusoidal terms, respectively. Figure 2 shows the shape functions (27) and (29) at arbitrary amplitudes. These satisfy the boundary conditions and symmetry requirements of the problem

$$\bar{w}(\bar{r}=0)=\bar{w}_{\mathrm{tot}} \qquad \bar{w}(\bar{r}=1)=0 \qquad \theta_r(\bar{r}=0)=0 \qquad \theta_r(\bar{r}=1)=0 \qquad \theta_r(\bar{r}=0)=0. \tag{30}$$

where $\bar{w}=w_{tot}/R$ and $\theta_r=\gamma_{rz}-\dfrac{\partial w}{\partial r}$ (see eq.(3)). The four additional DOFs introduced in Phase 2 are the shear deformation amplitudes associated with the first and second higher-order mode shapes, γ_{rz1} and γ_{rz2}, respectively, as well as the corresponding non-dimensional deflection amplitudes defined as deflections

$$\bar{w}_1=\frac{w_1}{R} \qquad\qquad \bar{w}_2=\frac{w_2}{R}. \tag{31}$$

We now employ the Euler-Lagrange equations (20) and re-write the governing equations (23), (24) and (25) in terms of eqs. (27) and (29), resulting in six non-dimensional equations of motion (given in Appendix A) with respect to $\bar{t}=t\sqrt{E/\rho}/R$ which can be solved numerically for the histories $\bar{w}_0(\bar{t})$, $\bar{w}_1(\bar{t})$, $\bar{w}_2(\bar{t})$, $\gamma_{\mathrm{rz0}}(\bar{t})$, $\gamma_{\mathrm{rz1}}(\bar{t})$ and $\gamma_{\mathrm{rz2}}(\bar{t})$ after imposing the following set of initial conditions

$$\begin{array}{ccc}
\bar{w}_0(\bar{t}_1)=\bar{w}_{0,\mathrm{t1}} & \bar{w}_1(\bar{t}_1)=0 & \bar{w}_2(\bar{t}_1)=0 \\
\dot{\bar{w}}_0(\bar{t}_1)=\dot{\bar{w}}_{0,\mathrm{t1}} & \dot{\bar{w}}_1(\bar{t}_1)=\bar{v}_{1,0} & \dot{\bar{w}}_2(\bar{t}_1)=\bar{v}_{2,0} \\
\gamma_{\mathrm{rz0}}(\bar{t}_1)=\gamma_{\mathrm{rz0,t1}} & \gamma_{\mathrm{rz1}}(\bar{t}_1)=0 & \gamma_{\mathrm{rz2}}(\bar{t}_1)=0 \\
\dot{\gamma}_{\mathrm{rz1}}(\bar{t}_1)=0 & \dot{\gamma}_{\mathrm{rz2}}(\bar{t}_1)=0 & \dot{\gamma}_{\mathrm{rz0}}(\bar{t}_1)=\dot{\gamma}_{\mathrm{rz0,t1}}
\end{array} \tag{32}$$

Here, the indices including ‘t1’ denote variables evaluated from the Phase 1 solutions at time $\bar{t}=\bar{t}_1$.

The initial (non-dimensional) velocities $\bar{v}_{1,0}$ and $\bar{v}_{2,0}$ (eq. (32)), corresponding to the initial amplitudes of the higher-order deflection modes, were determined such to satisfy conservation of kinetic energy between the two phases of response

$$T_{\mathrm{t1}}^{\mathrm{P1}}=T_{\mathrm{t1}}^{\mathrm{P2}} \tag{33}$$

where $T_{\mathrm{t1}}^{\mathrm{P1}}$ represents the kinetic energy of the plate at the end of Phase 1, $t=t_1$, and is given by

$$T_{\mathrm{t1}}^{\mathrm{P1}} = \pi\mu\left(0.214 w_{0,\mathrm{t1}}^2 \dot{\zeta}_{\mathrm{t1}}^2 + 0.171 w_{0,\mathrm{t1}} \dot{w}_{0,\mathrm{t1}} \zeta_{\mathrm{t1}} \dot{\zeta}_{\mathrm{t1}} + 0.0857 \dot{w}_{0,\mathrm{t1}}^2 \zeta_{\mathrm{t1}}^2\right) + \frac{1}{2} M \dot{w}_{0,\mathrm{t1}}^2 \tag{34}$$

while, at the beginning of the ensuing Phase 2 response, the kinetic energy reads

$$T_{\mathrm{t1}}^{\mathrm{P2}} = \frac{R^2\mu}{75600\pi^3}\begin{bmatrix} 6480\pi^4 \dot{w}_{0,\mathrm{t1}}^2 + 113400\pi^4 \dot{w}_{0,\mathrm{t1}}\left(v_{1,0}+v_{2,0}\right) + 14175\pi^4\left(v_{1,0}^2+v_{2,0}^2\right) + \\ +18900 v_{1,0}\left(\pi^4 v_{2,0} + \pi^2 \dot{w}_{0,\mathrm{t1}}\right) - 8400\pi^2 v_{2,0}\left(v_{1,0}+v_{2,0}\right) + 30912\pi^2 v_{1,0} v_{2,0} + \\ +226800 \dot{w}_{0,\mathrm{t1}} v_{1,0} + 11200 \dot{w}_{0,\mathrm{t1}} v_{2,0} \end{bmatrix} + \tag{35}$$

$$+\frac{1}{2} M\left(\dot{w}_{0,\mathrm{t1}} + v_{2,0}\right).$$

Now assume identical initial velocities for both higher-order modes

$$v_{1,0} = v_{2,0} = v_{12,0}. \tag{36}$$

Combining eqs. (33)-(36) allows one to solve for the common initial velocity $v_{12,0}$.

Experiments and simulations show that, upon reaching the plate boundary, the flexural wave is reflected towards the plate centre; we do not model explicitly such reflection but we introduce additional degrees of freedom to represent the excitation of high-order vibration modes, enforcing conservation of kinetic energy across the two phases of response.

2.2 Deformation modes

In this section we proceed to examine the deformation behaviour during both phases of the response (see Section 2.1). Recalling eq. (5), we note that the magnitude of the average radial strain

$$\bar{\varepsilon}_{rr} = \frac{1}{R}\int_0^R \varepsilon_{rr}(r)\,dr \tag{37}$$

increases, in a first approximation, with the ratio of centre deflection to the position of the flexural wave front; thus we define

$$\beta(t) = \begin{cases} w_0(t)/\zeta(t) & t \le t_1 \\ w_{\mathrm{tot}}(t)/R & t > t_1 \end{cases} \tag{38}$$

It can be seen from eq. (38) that the time histories of $\beta(t)$ are strongly affected by the flexural wave propagation process: if the flexural wave speed $\dot{\zeta}$ is low compared to the transverse plate velocity $\dot{w}_0$, $\beta_{\max} = \max\left[\beta(t)\right]$ is likely to be reached in the early phase of the response, indicating that the peak value of $\bar{\varepsilon}_{rr}$ (eq.(37)) may occur during Phase 1, i.e.

$t \le t_1$, thus promoting early penetration of the plate in the wave-controlled phase; on the other hand, if $\dot{\zeta} \ll \dot{w}_0$, the peak strains are more likely to occur in the boundary-controlled Phase 2 response $\left(t > t_1\right)$. Accordingly, two characteristic deformation modes can be identified in this context:

- *Mode 1:* $\beta_{\max}$ is reached in Phase 2, i.e. in the boundary-controlled phase of the response; the peak strains and failure mechanisms will depend strongly on the boundary conditions (e.g. plate size).
- *Mode 2:* $\beta_{\max}$ is reached in Phase 1, i.e. in the wave-controlled phase of the response; the peak strains and failure mechanisms will be less sensitive to boundary conditions.

It merits comment that the above classification is based on the assumption that the composite fails by a tensile fibre failure mechanism. While in the case of extreme impact velocities, localised transverse shear failure is often the dominant failure mode [8], the two deformation modes defined above are more relevant to problems at the lower end of the high-velocity impact range (approximately 50 – 300 ms^{-1}).

In Fig. 3 we plot a mode transition map in the $\bar{M} - \bar{h}$ space for the case of elastic, isotropic plates with $\nu = 0.25$, hence $\bar{G} = 1 \big/ \left[2\left(1+\nu\right)\right] = 0.4$; the contours in Fig. 3 denote the mode transitions for fixed values of non-dimensional impact velocity, $\bar{v}_0$. While extremely low mass ratios $\bar{M}$ cause Mode 2 to dominate, the effect of increasing $\bar{M}$ is to extend the Mode 2 domain to smaller $\bar{h}$ values; it can also be seen that if $\bar{M} > 1.2$, Mode 2 deformation is fully suppressed for any choice of $\bar{v}_0$. If $\bar{M} < 1.2$, an increase in $\bar{v}_0$ promotes a Mode 2 response. While the transition map presented in Fig. 3 is valid for plates of arbitrary stiffness *E*, strictly speaking, it is limited to the choice of $\nu = 0.25$. However, our calculations suggest that the sensitivity of the map in Fig. 3 to variations of the Poisson's ratio is small in the practical range $0 < \nu < 0.5$.

3. Finite element models

Three-dimensional dynamic FE simulations were performed using ABAQUS/Explicit to validate the analytical model derived above. The FE models consisted of two components, a spherical rigid projectile of radius R_s and mass M and a circular orthotropic plate of radius R and thickness h; unless otherwise stated, $R = 50\,\text{mm}$ and $R_s = 5\,\text{mm}$.

The circular plate was discretised using four-noded quadrilateral shell elements with reduced integration (S4R in ABAQUS). In the radial direction, the element size was approximately 1.5 mm, while 60 elements were used to discretise the plate along the circumferential direction. In order to accurately resolve the strain gradients at the impact point, a finer mesh (element size 0.5 mm) was used for a central patch of radius 6 mm surrounding the point of first impact. The projectile was modelled as a spherical, rigid surface with its centre of mass located such to coincide with the *z*-axis.

Two different composite laminates were modelled:

a) <u>Carbon-fibre/epoxy laminates (CFRP).</u>
   We considered cross-ply and quasi-isotropic CFRP laminates comprising of unidirectional AS4/epoxy plies [26] each of thickness $h_l = 0.125\,\text{mm}$ and density $\rho = 1580\,\text{kgm}^{-3}$; the elastic lamina properties were taken from [26] and are listed in Table 1. The layups of the cross-ply laminates were chosen to be symmetric, $[0,90]_{ns}$, where *n* was either 2, 5 or 10 to obtain laminates of total thicknesses *h* = 1 mm, 2.5 mm and 5 mm, respectively. The quasi-isotropic laminate had a total thickness of $h = 5\,\text{mm}$ and stacking sequence $[0,45,90,-45]_{5s}$.

b) <u>Glass-fibre/epoxy laminates (GFRP).</u>
   The GFRP laminates considered here comprised unidirectional E-glass/epoxy plies, each of thickness $h_l = 0.125\,\text{mm}$ as for the CFRP plates but with a higher density of $\rho = 2030\,\text{kgm}^{-3}$. The mechanical properties of the GFRP laminae (also taken from [26]) are included in Table 1. The same stacking sequences as for the CFRP are analysed in the case of the GFRP.

The laminate was modelled in ABAQUS as a stack of transversely isotropic laminae by using the built-in *composite shell section*; this approach is convenient because ABAQUS automatically computes the laminate’s stiffness matrix from the specified ply thickness, stacking sequence and material properties according to laminate theory. In this study, attention is restricted to the elastic response of composites and therefore, damage and failure mechanisms are not considered in the FE calculations.

Simulations were also performed on isotropic plates with density, Young's modulus and Poisson's ratio chosen as $\rho = 1700\,\mathrm{kgm^{-3}}$, $E = 50\,\mathrm{GPa}$ and $\nu = 0.25$, respectively. In these simulations, an axisymmetric modelling approach was employed: the plate was meshed with 150 elements in the radial direction and 20 elements in the through-thickness direction using 4-noded axisymmetric elements with reduced integration (CAX4R in ABAQUS).

In both 3D and axisymmetric FE models the plate was fully clamped along its periphery, with all DOFs constrained to zero. Impact loading was performed by imparting an initial velocity v_0 to the projectile. Contact between the plate and projectile was assumed to be frictionless and was modelled in ABAQUS using a surface-to-surface contact based on the penalty contact method with a finite sliding formulation; both plate and projectile were permitted to move independently subsequent to contact separation.

In the following we compare the numerical and analytical predictions and explore the two characteristic deformation mechanisms defined in Section 2.2.

4. Comparison of analytical and FE predictions

In this section, analytical and FE predictions of centre deflection versus time histories are compared in order to validate the analytical models, to explore the two characteristic deformation modes and to examine the sensitivity of the dynamic response to the governing non-dimensional parameters (eq. (22)). In addition, the sensitivity of plate deflection to variations of projectile size will be explored and discussed. Initially, we focus on isotropic material behaviour, in order to compare the two types of predictions in absence of any inaccuracy caused by the axisymmetric idealisation employed in the analytical models. Subsequently we probe the accuracy of our analytical models to predict the elastic response of the CFRP and GFRP laminates (see Section 3) by comparing their predictions to those obtained from detailed dynamic FE simulations.

4.1 Response of isotropic plates

4.1.1 Deflection versus time histories

Analytical and FE predictions of centre deflection versus time are compared in this section for the case of fully isotropic elastic plates. Two axisymmetric FE simulations were performed with $E = 50\,\text{GPa}$ and $\nu = 0.25$ ($\bar{G} = 1\big/\left[2\left(1+\nu\right)\right] = 0.4$), and the plate thickness *h*, the projectile mass *M* and the impact velocity v_0 were chosen to obtain two different sets of non-dimensional parameters $\bar{h}$, $\bar{M}$ and $\bar{v}_0$, corresponding to the two deformation modes described in Section 2.2.

In Fig. 4a, analytical and FE predictions of the normalised local deformation parameter $\beta = w_0/\zeta$ (38) are plotted as functions of the non-dimensional time, $\bar{t} = t\sqrt{E/\rho}/R$, for the choice $\bar{h} = 0.1$, $\bar{M} = 0.6$ and $\bar{v}_0 = 0.04$. We also include in this figure predictions obtained from a reduced analytical model that ignores the excitation of the additional sinusoidal mode shapes during Phase 2 response; the governing equations for this reduced model can be readily obtained by setting $\bar{w}_1 = \bar{w}_2 = \gamma_{\text{rz}1} = \gamma_{\text{rz}2} \equiv 0$ in eqs. (39)-(44), see Appendix A. According to the mode transition chart presented in Fig. 3, this choice of non-dimensional parameters should give rise to a Mode 1 behaviour, as indicated by the respective marker, and the predictions presented in Fig. 4a confirm this, with β reaching its peak during the Phase 2 response,

$\bar{t} > \bar{t}_1$.

In Fig. 4b, the same predictions are plotted in a normalised centre deflection $\bar{w}_0 = w_0/R$ versus $\bar{t}$ chart, showing excellent agreement between the FE and analytical predictions. On the other hand the reduced model significantly under-predicts the deflection of the plate (this reduced model does not enforce conservation of kinetic energy across the transition from Phase 1 to Phase 2).

Figure 4c presents the corresponding predictions of normalised flexural wave position, $\bar{\zeta} = \zeta/R$, as functions of $\bar{t}$. Note that the FE predictions of $\bar{\zeta}\left(\bar{t}\right)$ were determined from the deformed plate contours by tracing the position of the elastic hinge, defined at the point where the slope of the deformed middle-surface in *r*-direction is zero. It can be seen from Fig. 4c that the analytical and FE predictions are in good agreement, suggesting that the proposed analytical model adequately captures the details of the flexural wave propagation mechanism associated with Mode 1 behaviour. The analytical calculations also showed that, short after the impact had occurred, the speed of the flexural wave, $\dot{\zeta}$, was approximately equal to the shear wave speed in the elastic solid, $c_s = \sqrt{G/\rho} = 3430\,\mathrm{ms}^{-1}$, and quickly dropped to reach a constant speed of $\dot{\zeta} = 950\,\mathrm{ms}^{-1}$.

In Fig. 5a we compare FE and analytical predictions of the $\beta = w_0/\zeta$ versus $\bar{t}$ response corresponding to the choice $\bar{h} = 0.05$, $\bar{M} = 0.05$ and $\bar{v}_0 = 0.04$. It can be seen from Fig. 3 that this set of non-dimensional parameters results in a Mode 2 deformation response, and both types of predictions included in Fig. 5a show that this is the case, with $\beta_{\max}$ reached clearly in the Phase 1 response, $\bar{t} < \bar{t}_1$. The corresponding $\bar{w}_0 = w_0/R$ versus $\bar{t}$ traces are illustrated in Fig. 5b. While the agreement between analytical and FE predictions is satisfying in the Phase 1 response, larger discrepancies occur in the ensuing Phase 2 response, in which the FE model predicts rapid transverse oscillations which are not picked up by the analytical model due to the limited number of mode shapes considered in this phase of response. However, the peak centre deflections, $\bar{w}_0^{\max} = \max(w_0/R)$, as predicted by the FE and analytical model, respectively, are found in good agreement, while the reduced analytical model, again, substantially under-predicts the FE results of $\bar{w}_0^{\max}$. However recalling that, for the case of a Mode 2 response, the onset of fibre failure is achieved during Phase 1 ($\bar{t} < \bar{t}_1$), these discrepancies are not relevant for the prediction of damage initiation.

In Fig. 5c, we present the corresponding analytical and numerical predictions of $\bar{\zeta} = \zeta/R$ as functions of $\bar{t}$. Good correlation between both types of predictions is achieved for the initial phase of response, the flexural wave speed starts to slow down at $\bar{t} \approx 1.5$ in the FE results, while the analytical model predicts a nearly constant wave speed of $\dot{\zeta} = 960\,\mathrm{ms}^{-1}$ until the end of the Phase 1 response, at $\bar{t} = \bar{t}_1$. However, the agreement between the two types of predictions is still reasonably satisfactory.

Analytical and FE predictions of normalised deflection profiles are compared in Figs. 6a and 6b for the two cases presented in Figs. 4 and 5, respectively; the two snapshots presented in each figure are taken before and after the flexural wave had reached the plate boundary (i.e. transition between Phase 1 and 2). Figure 6a shows that the analytical model adequately captures the FE predictions of the deflection profile during both phases of this Mode 1 type of response. For Mode 2 behaviour, analytical and FE predictions are in good agreement during the initial phase of response (i.e. for $\bar{t} = 0.76$, Phase 1), as seen from Fig. 6b. On the other hand, during Phase 2, the FE predictions show that plate deflection is dictated by higher order mode shapes which are not accurately captured by the analytical model due to the limited vibrational modes considered in eq. (27). However, for this Mode 2 type of response, the peak strains are expected to occur early in Phase 1 (see Section 2.2) and therefore, from a failure perspective, the discrepancies in plate deflection for $\bar{t} = 6.2$ are of minor relevance.

4.1.2 Sensitivity of the dynamic response to non-dimensional parameters

In this section, the analytical model is employed to examine, for the case of isotropic material behaviour ($E = 50\,\text{GPa}$, $\nu = 0.25$, $\bar{G} = 0.4$), the sensitivity of the plate's deflection response to the governing non-dimensional parameters (eq. (22)).

In Fig. 7a, analytical predictions of the normalised peak deflections, $\bar{w}_{\max} = \max\left(w_0/R\right)$ and $\beta_{\max} = \max\left(w_0/\zeta\right)$, are presented as functions of the non-dimensional impact velocity $\bar{v}_0 = v_0\sqrt{\rho/E}$ for the choice $\bar{M} = 0.05$; contours of aspect ratio $\bar{h} = h/R$ are included for three different values 0.02, 0.05 and 0.1, respectively. For comparison purposes, we also include in Fig. 7a predictions of $\beta = w_0/\zeta$ obtained from corresponding FE simulations (indicated by triangles, diamonds and circles). It can be seen from Fig. 7a that for some ranges, the analytical predictions of the peak values of $\bar{w}_0$ and β coincide, indicating Mode 1 behaviour, while those with $\bar{w}_0 \neq \beta$ are associated with a Mode 2 response, in line with the transitions plotted in Fig. 3. Both FE and analytical predictions are found in excellent agreement and show that the effect of increasing $\bar{v}_0$ is to monotonically increase both $\bar{w}_0$ and β for each choice of $\bar{h}$, and the slope of the $\bar{h}$-contours in the β-$\bar{v}_0$ space increases with decreasing value of $\bar{h}$, while in the $\bar{w}_0$-$\bar{v}_0$ space, the different $\bar{h}$-contours are almost parallel. In addition, Fig. 7a shows that larger aspect ratios lead to smaller values of $\bar{w}_0$ and β.

Similar information is presented in Fig. 7b for the case of a much higher non-dimensional projectile mass, $\bar{M} = 0.6$. For this choice of $\bar{M}$ the analytical predictions of $\bar{w}_0 = w_0/R$ and

$\beta = w_0/\zeta$ coincide almost over the entire range shown in Fig. 7b, indicating that Mode 1 behaviour is predominantly active. It can be seen from Fig. 7b that Mode 2 behaviour is active only in case of thin plates, $\bar{h} = 0.02$, impacted at very high velocities, $\bar{v}_0 > 0.022$; this transition can be attributed to (i) the slowing flexural wave associated with a decrease of plate thickness, and (ii) the increase in the ratio $\beta = w_0/\zeta$ when the impact velocity is increased, effectively promoting a Mode 2 response. Note that these observations are in line with the regime transitions plotted in Fig. 3. In Fig. 7b, the observed trends are similar to those obtained for the $\bar{M} = 0.05$ case (compare Fig. 7a), and the analytical predictions are again in excellent agreement with those obtained from the FE simulations.

4.1.3 Influence of projectile dimensions on the deflection response

We proceed to examine the sensitivity of plate deformation to variations of projectile dimensions, as quantified here by the normalised projectile radius, $\bar{R}_s = R_s/R$. First, it should be clarified that the effects of $\bar{R}_s$ are not accounted for in our analytical models and therefore we shall restrict this study to the use of the FE method.

Axisymmetric FE simulations were performed on isotropic plates ($E = 50\,\text{GPa}$, $\nu = 0.25$, $\bar{G} = 0.4$) and the normalised projectile radius, $\bar{R}_s$, was varied between 0.04 to 0.5, while the parameters $\bar{M} = 0.6$ and $\bar{v}_0 = 0.022$ were held fixed; the aspect ratio $\bar{h} = h/R$ was either 0.05 or 0.1. Figure 8 reports the predicted sensitivity of the normalised peak centre deflection $\bar{w}_{\max} = \max(w_0/R)$ to variations of the normalised projectile radius, $\bar{R}_s$, for the two choices of $\bar{h}$; analytical predictions corresponding to the chosen sets of non-dimensional parameters are included for comparison and show no sensitivity to $\bar{R}_s$, as expected. It can be seen from the FE predictions that variations in $\bar{R}_s$ only play a minor role in the elastic deformation response, justifying the fact that in our analytical model the contact indentations was neglected.

4.2 Response of composite plates

Having demonstrated that our analytical models are accurate for the isotropic case, we now proceed to examine the response of composite plates. The sensitivity of the predicted response to variations of composite layup are investigated.

4.2.1 Deflection versus time histories

With reference to Fig. 9, consider clamped circular composite plates of radius $R = 50\,\text{mm}$ and thickness $h = 2.5\,\text{mm}$, made from a CFRP laminate. The plates are subject to impact loading by a rigid spherical projectile of mass $M = 3.1\text{g}$ and radius $R_s = 5\,\text{mm}$, travelling at velocity $v_0 = 86\,\text{ms}^{-1}$. The corresponding analytical and FE predictions of centre deflection versus time histories are included in Fig. 9a for two different layup choices of equal thickness and areal mass, $[0,45,90,-45]_{2s}$ (lamina thickness of 0.156 mm, dotted curves) and $[0,90]_{5s}$ (lamina thickness of 0.125 mm, continuous curves). In the analytical calculations, eq. was employed to calculate, for both types of laminate, the effective Young's modulus $\tilde{E}_r$, Poisson's ratio $\tilde{\nu}_{r\varphi}$ and transverse shear modulus $\tilde{G}_r$, as listed in Table 2. Figure 9a shows that the peak centre deflection, $w_{\max}$, is found to be in good agreement between analytical and FE predictions. For the quasi-isotropic laminate, the FE model predicts a slightly lower peak deflection compared to the cross-ply layup, and the analytical predictions follow this trend.

The corresponding predictions of flexural wave position versus time histories $\zeta(t)$ are presented in Fig. 9b; the dashed and solid curves in this figure represent the analytical predictions, and the FE results are indicated by full and empty circles, respectively. Note that the FE results of $\zeta(t)$ were obtained by tracing the position of the flexural wave front along the 0°-direction of the laminate. The analytical predictions show that the flexural wave speed associated to the response of the cross-ply laminate is slightly lower than that of the quasi-isotropic laminate owing to the lower effective Young's modulus, $\tilde{E}_r$, of the cross-ply layup (see Table 2), and the FE predictions confirm this scenario.

The predictions presented in Figs. 9a and 9b were used to plot time histories of $\beta = w_0/\zeta$, as illustrated in Fig. 9c. Both types of predictions show that the initial peak in $\beta(t)$ during the

Phase 1 response ($t < t_1$) is smaller than that found in Phase 2, hence this response is associated to Mode 1 behaviour (see Fig. 3). It can be seen from Fig. 9c that the analytical predictions of both peaks are found in good correlation with those predicted by the FE models.

4.2.2 Sensitivity of the dynamic response to non-dimensional parameters

We proceed to examine the effects of the non-dimensional parameters (22) on the deflection response of laminated composites. For this study, analytical calculations were conducted on CFRP laminates with lay-up $[0,90]_{ns}$ and radius $R = 50\,\text{mm}$ (see Section 3 for mechanical properties), and the laminate thickness h, the impact velocity v_0 and the projectile mass M were varied in order to construct non-dimensional response maps similar to those presented in Fig. 7 for the case of isotropic plates.

Figure 10 presents two such maps in which analytical predictions of non-dimensional peak deflections, $\bar{w}_{\max} = w_{\max}/R$ (dashed curves), and maximum local deformation, $\beta_{\max} = w_{\max}/\zeta$ (solid curves), are plotted as functions of the non-dimensional impact velocity $\bar{v}_0$ for the choices $\bar{M} = 0.05$ (Fig. 10a) and $\bar{M} = 0.1$ (Fig. 10b), with contours of aspect ratio $\bar{h} = h/R$ included. Also included in this figure are FE predictions of $\beta_{\max}$ obtained for selected points within the range considered here, in order to provide further validation of the analytical models. The two charts illustrated in Fig. 10 show similar response characteristics as those presented in Fig. 7 for the isotropic case, and the analytical predictions are found in excellent agreement with the results obtained from the FE simulations, which gives us confidence that our analytical models are adequate to represent the dynamic deformation response of composite laminates subject to ballistic impact.

5. Onset of failure

Having established the accuracy of the analytical predictions, the models are now employed to determine the onset of tensile failure. Impact experiments on fibre-reinforced composite plates (see e.g. Heimbs et al. [3]) have shown that fibre failure can initiate at the distal face of the laminate at impact velocities much below the ballistic limit, leading to a degradation of stiffness which can appreciably affect the plate's dynamic response. The analytical models presented herein do not account for such failure processes; however, they can be used to predict their first occurrence by considering a strain-based failure criterion, which is the scope of this section. In the case of impact from a projectile with general shape it is likely that composite plates may suffer localised damage in the proximity of the contact point. In what follows, we assume that such localised damage does not appreciably affect the stiffness of the composite plate, i.e., contact damage is sufficiently restricted to a small area around the impact point.

Before studying the failure behaviour of the laminated plates, it is necessary to assess the accuracy of the strain predictions provided by our analytical model. To do this we first compare analytical strain predictions to those obtained from detailed FE simulations and explore their sensitivity to variations of projectile dimensions. Then, a strain-based damage initiation criterion is stated to compare the impact resistance of typical CFRP and GFRP plates, and finally, we construct non-dimensional design charts which can be used to determine the onset of tensile failure for both types of laminates.

5.1 Time histories of fibre strain

Finite element simulations were performed on a CFRP plate of thickness $h = 2.5\,\text{mm}$, radius $R = 50\,\text{mm}$ and lay-up $[0,90]_{5s}$ (see Table 2) subject to impact at $v_0 = 86\,\text{ms}^{-1}$ by a ball projectile of mass $M = 3.1\,\text{g}$, giving $\bar{M} = 0.1$, $\bar{v}_0 = 0.016$ and $\bar{h} = 0.05$; the normalised projectile radius $\bar{R}_s = R_s/R$ was either 0.05, 0.1 or 0.2 in these calculations. Figure 11a presents the predicted time histories of radial fibre strain induced in the distal face of the laminate below the impact point, $\varepsilon_1(t)$; we also include in this figure the corresponding analytical predictions of $\varepsilon_1(t)$ which are insensitive to $\bar{R}_s$. The obtained predictions show that the strain rapidly rises and soon reaches a peak value, $\varepsilon_{1,\max}$, followed by a more moderate decay. The FE predictions in Fig. 11a show that the variations of the normalised plate radius, $\bar{R}_s$, have small effect on the strain response, $\varepsilon_1(t)$, for the range of $\bar{R}_s$ considered here; the corresponding analytical prediction follows a similar trend and its peak value, $\varepsilon_{1,\max}$, is found in good correlation with the FE results. With the above loading conditions, the predicted $\varepsilon_{1,\max}$ values are higher than the quasi-static tensile ductility, $\varepsilon_{1T}^{*} = 1.38\%$ [26], shown in Figs. 11a and 11b as a reference.

The FE predictions plotted in Fig. 11a also show that $\varepsilon_{1,\max}$ is reached approximately 15 μs after the first contact with the projectile has occurred. This raises questions whether the time histories presented in Fig. 11a are affected by propagation of the tensile precursor wave or whether radial equilibrium has been achieved, as assumed in our analytical model (see Section 2.1.3). This issue was clarified by tracing the propagation of the tensile precursor wave in radial direction of the composite plate, as predicted by the dynamic FE simulations. The results showed that the tensile wave reached the plate boundary 7 μs after the impact had occurred (average wave speed of 6900 ms^{-1}); hence, the tensile wave only reflected once from the fixed boundary before $\varepsilon_{1,\max}$ was reached in Fig. 11a. However, further examination of the stress field in the plate revealed that the magnitude of the tensile wave during $0 < t < 40$ μs was negligible compared to the bending stresses induced through propagation of the flexural wave; this can be justified by the vanishingly small membrane stresses induced in the plate during this phase of response (the plate deflection was less than 1.5 mm).

Figure 11b shows analytical and FE predictions of peak strain $\varepsilon_{1,\max}$ as functions of non-dimensional impact velocity $\bar{v}_0 = v_0\sqrt{\rho / \tilde{E}_r}$ and reveals a nearly linear relationship between both quantities. It can also be seen from this figure that the effect of the projectile dimension, represented by $\bar{R}_s = R_s/R$, is more pronounced when the impact velocity $\bar{v}_0$ is higher.

If we assume that the composite shows signs of failure at the distal face when $\varepsilon_{1,\max} > \varepsilon_{1T}^{\ *}$, we find a critical impact velocity at the inception of failure of $v_0^* = 43\,\mathrm{ms}^{-1}$ (or $\bar{v}_0^* = 0.008$ in non-dimensional terms); this, as expected, is significantly lower than the ballistic limit v_L, reported in the literature for a similar type of laminate (e.g. Cunniff [12] reports $v_L \approx 150\,\mathrm{ms}^{-1}$ for the case of a CFRP laminate).

The choice of identifying the limiting tensile strain with the measured quasi-static tensile ductility $\varepsilon^{*}_{\ 1T}$ of the composite is obviously only a first approximation; such limiting strain is expected to be influenced by the applied strain rate, the details of the strain field, the sensitivity of the measured tensile ductility to gauge size. Our calculation provide effective predictions of the peak tensile strain in the laminate; these may be used as inputs for more complex failure models, but this is not pursued in this study.

5.2 Damage resistant design of CFRP and GFRP plates

The validated analytical model is now used to explore the damage resistance of CFRP and GFRP laminates, as quantified by the critical velocity, v_0^*, at which the failure strain, $\varepsilon_{1\mathrm{T}}^*$, is reached at the tensile face. In Fig. 12 we present analytical predictions of maximum fibre strain, $\varepsilon_{1,\max}$, induced in CFRP and GFRP plates with equal mass and layup $[0,90]_{\mathrm{ns}}$, as functions of v_0 for the choice $\bar{M} = 0.05$; contours of aspect ratio $\bar{h} = 0.04$ and $\bar{h} = 0.08$ are included for each laminate. The predictions show that the choice of $\bar{h}$ has vanishing effect on the magnitude of $\varepsilon_{1,\max}$ for a given type of laminate and that the response of the GFRP plates is associated to larger values of $\varepsilon_{1,\max}$ compared to CFRP plates impacted at equal velocities; this can be justified by the lower equivalent stiffness, $\tilde{E}_r$, of the GFRP laminates, see Table 2. However, taking into account the higher quasi-static ductility of the GFRP laminate, $\varepsilon_{1\mathrm{T}}^* = 2.8\%$ (Table 1), it follows that the critical velocities, v_0^*, of the GFRP laminates are approximately 30 % higher than those predicted for the stiffer (and more brittle) CFRP plates ($\varepsilon_{1\mathrm{T}}^* = 1.38\%$, see Table 1), which allows concluding that GFRP composites generally outperform CFRP laminates in terms of damage resilience.

We now employ the analytical model to determine damage-resistant plate designs and construct design charts in the $\bar{h}$ - $\bar{M}$ - space, for the practical ranges $0.01 \le \bar{M} \le 1$ and $0.02 \le \bar{h} \le 0.14$. Figure 13a presents such a map for the case of CFRP cross-ply laminates ($[0,90]_{\mathrm{ns}}$, $\bar{G} = \tilde{G}_r / \tilde{E}_r = 0.12$, $\tilde{\nu}_{r\varphi} = 0.15$, see Table 2); we include in Fig. 13a contours of non-dimensional critical impact velocity, $\bar{v}_0^*$, defined as the velocity at which the maximum tensile strain in the laminate reaches the failure strain of the CFRP material, $\varepsilon_{1,\max} = \varepsilon_{1\mathrm{T}}^* = 1.38\%$ (Table 1). Note that the area left to each $\bar{v}_0^*$ - contour represents the design space $\{\bar{h}, \bar{M}\}$ in which the laminate can safely withstand ballistic impact without fibre damage, i.e. $\varepsilon_{1,\max} < \varepsilon_{1\mathrm{T}}^*$. In Fig. 13b we present a similar design map for the case of GFRP cross-ply laminates ($[0,90]_{ns}$, $\bar{G} = 0.24$, $\tilde{\nu}_{r\varphi} = 0.26$, see Table 2) with higher ductility, $\varepsilon_1^{\max} = \varepsilon_{1T}^* = 2.8\%$ (Table 1).

6. Conclusions

We developed and validated a physically based model for predicting the dynamic deformation of fully clamped, circular elastic composite plates subject to impact by a rigid projectile. The mathematical framework is based on first-order shear deformation theory of plates and takes into account large deformation, propagation of flexural waves as well as higher-order vibrational modes emerging in the boundary-controlled phase of response; local indentation and damage at the contact point are not explicitly modelled, which limits the applicability of the model to thin plates impacted by relatively blunt projectiles. The constitutive response of the composite was linear elastic with effective stiffness deduced from the stiffness matrix of the laminate; the mathematical formulation of plate deflection was based on axisymmetric shape functions assumed a-priori. This approach yields a set of nonlinear ODEs which can be solved using common numerical integration methods.

The dynamic response was found to be governed by only four non-dimensional parameters, namely $\bar{h}$, $\bar{M}$, $\bar{v}_0$ and $\bar{G}$, representing aspect ratio, mass ratio, non-dimensional impact velocity and transverse shear stiffness, respectively. Two characteristic deformation modes were identified and non-dimensional transition maps were constructed.

The analytical models were validated by comparing their predictions to those of detailed dynamic FE simulations and a good correlation was found for a wide range of plate geometries, projectile masses and impact velocities. It was shown that neglecting additional vibrational modes during the boundary-controlled phase of the response can lead to under-predictions of the plate's centre deflection and peak strain. In addition, detailed FE simulations showed that the deflection response of elastic plates is only mildly sensitive to the projectile radius.

The sensitivity of peak tensile strain to variations of the (non-dimensional) projectile velocity was examined for two types of composites, (i) carbon-fibre/epoxy (CFRP) and (ii) glass-fibre/epoxy (GFRP) laminates. It was shown that tensile failure of plies may initiate early, in the wave-controlled phase of response, and the critical velocities associated to the inception of damage were found, as expected, below the measured limit velocities for full penetration. It was found that the GFRP plates can sustain higher impact velocities at the inception of failure compared to plates made from CFRP of equal mass, concluding that GFRP composites outperform stiffer and more brittle CFRP laminates in terms of impact damage resilience.

The critical velocity $\bar{v}_0^*$ provided by the calculations presented here can be interpreted as (1) a lower bound on the ballistic limit of the plate or (2) as an upper bound on the maximum impact velocity which a certain plate can sustain with no damage. The analytical models were used to construct design maps for both CFRP and GFRP laminates in order to aid the selection of damage-resistant plate geometries.

Acknowledgements

The authors would like to thank EPSRC for funding through the Doctoral Prize Fellowship scheme.

Appendix A. Governing equations for the Phase 2 response

The governing equations for the Phase 2 response ($t > t_1$) are obtained in terms of eqs. (27) and (29) by employing the Euler-Lagrange equations (20), and are given by

$$\frac{1}{945\pi^3}\begin{bmatrix} 3780\pi^4\bar{M}\left(\ddot{\bar{w}}_0+\ddot{\bar{w}}_2\right)+567\pi^4\left(\ddot{\bar{w}}_1+\ddot{\bar{w}}_2\right)+648\pi^4\ddot{\bar{w}}_0+945\pi^2\ddot{\bar{w}}_1- \\ -420\pi^2\ddot{\bar{w}}_2+11340\ddot{\bar{w}}_1+560\ddot{\bar{w}}_2 \end{bmatrix}= \\ =-\frac{1}{\left(1-\tilde{\nu}_{r\varphi}^2\right)}\left[3\pi\bar{h}^2\left(\gamma_{\mathrm{rz0}}\bar{h}^2+4\bar{w}_0+2\bar{w}_2\right)+2\pi\bar{w}_0\left(5\bar{w}_0^2+9\bar{w}_2^2\right)+\bar{h}^2\left(2\gamma_{\mathrm{rz2}}-3\gamma_{\mathrm{rz1}}\right)\right], \tag{39}$$

$$1.086\left[0.19\ddot{\bar{w}}_0-0.345\ddot{\bar{w}}_1+0.268\ddot{\bar{w}}_2\right]= \\ =-\frac{0.0833}{\left(1-\tilde{\nu}_{r\varphi}^2\right)}\left[\bar{h}^2\left(2.82\gamma_{\mathrm{rz0}}-35.9\gamma_{\mathrm{rz1}}+17\gamma_{\mathrm{rz2}}+243.6\bar{w}_0+159.9\bar{w}_2\right)+120\bar{w}_0^3+216\bar{w}_0\bar{w}_2^2\right], \tag{40}$$

$$0.1403\ddot{\bar{w}}_0-0.291\ddot{\bar{w}}_1+0.352\ddot{\bar{w}}_2+\bar{M}\left(\ddot{\bar{w}}_0+\ddot{\bar{w}}_2\right)= \\ =-\frac{0.0833}{\left(1-\tilde{\nu}_{r\varphi}^2\right)}\begin{bmatrix} \bar{h}^2\left(-35.85\gamma_{\mathrm{rz0}}-25.45\gamma_{\mathrm{rz1}}+112.9\gamma_{\mathrm{rz2}}+177.9\bar{w}_0+1064.4\bar{w}_2\right)+ \\ +486\bar{w}_2^3+270\bar{w}_2\bar{w}_0^2 \end{bmatrix}, \tag{41}$$

$$0=\bar{h}^2\left(35.85\bar{w}_2-11.82\bar{w}_0-6.59\gamma_{\mathrm{rz0}}+0.449\gamma_{\mathrm{rz1}}+3.804\gamma_{\mathrm{rz2}}\right)-3.75\bar{G}\gamma_{\mathrm{rz0}}\left(1-\tilde{\nu}_{r\varphi}^2\right)+ \\ +0.597\bar{G}\gamma_{\mathrm{rz1}}\left(1-\tilde{\nu}_{r\varphi}^2\right)+0.424\bar{G}\gamma_{\mathrm{rz2}}\left(1-\tilde{\nu}_{r\varphi}^2\right), \tag{42}$$

$$0=\bar{h}^2\left(-38.76\bar{w}_0-25.45\bar{w}_2-0.449\gamma_{\mathrm{rz0}}+5.71\gamma_{\mathrm{rz1}}-2.70\gamma_{\mathrm{rz2}}\right)-0.597\bar{G}\gamma_{\mathrm{rz0}}\left(1-\tilde{\nu}_{r\varphi}^2\right)+ \\ +1.25\bar{G}\gamma_{\mathrm{rz1}}\left(1-\tilde{\nu}_{r\varphi}^2\right)-0.486\bar{G}\gamma_{\mathrm{rz2}}\left(1-\tilde{\nu}_{r\varphi}^2\right), \tag{43}$$

$$0=\bar{h}^2\left(18.88\bar{w}_0+112.9\bar{w}_2-3.804\gamma_{\mathrm{rz0}}-2.70\gamma_{\mathrm{rz1}}+11.98\gamma_{\mathrm{rz2}}\right)-0.424\bar{G}\gamma_{\mathrm{rz0}}\left(1-\tilde{\nu}_{r\varphi}^2\right)- \\ -0.486\bar{G}\gamma_{\mathrm{rz1}}\left(1-\tilde{\nu}_{r\varphi}^2\right)+1.25\bar{G}\gamma_{\mathrm{rz2}}\left(1-\tilde{\nu}_{r\varphi}^2\right). \tag{44}$$

References

[1] K.F. Graff, Wave motion in elastic solids, Clarendon Press, Oxford, 1975.

[2] N. Takeda, R.L. Sierakowski, C.A. Ross, L.E. Malvern, Delamination-crack Propagation in Ballistically Impacted Glass/Epoxy Composite Laminates, Exp. Mech., 22 (1982) 19-25.

[3] S. Heimbs, T. Bergmann, D. Schueler, N. Toso-Pentecote, High velocity impact on preloaded composite plates, Compos. Struct., 111 (2014) 158-168.

[4] F.K. Chang, K.Y. Chang, A progressive damage model for laminated composites containing stress concentrations, J Compos Mater, 21 (1987) 834-855.

[5] H. Matsumoto, Y. Ogawa, T. Adachi, Stress Analysis of an Orthotropic Laminated Slab Subject to a Transverse Load, JSME Int J I-Solid M, 35 (1991) 165-169.

[6] E. Wu, C.Z. Tsai, Impact behaviour and analysis of CFRP laminated plates, in: S.R. Reid, G. Zhou (Eds.) Impact behaviour of fibre-reinforced composite materials and structures, Woodhead Publishing Ltd., Cambridge, 2000.

[7] S. Abrate, Impact on Laminates Composites: Recent Advances, Appl. Mech. Rev., 47 (1994) 517-544.

[8] W.J. Cantwell, J. Morton, Impact Perforation of Carbon Fibre Reinforced Plastic, Compos Sci Technol, 38 (1990) 119-141.

[9] H.M. Wen, Predicting the penetration and perforation of FRP laminates struck normally by projectiles with different nose shapes, Compos. Struct., 49 (2000) 321-329.

[10] R.A.W. Mines, A.M. Roach, N. Jones, High velocity perforation behaviour of polymer composite laminates, Int. J. Impact Eng., 22 (1999) 561-588.

[11] G. Zhu, W. Goldsmith, C.K.H. Dharan, Penetration of laminated Kevlar by projectiles - I. Experimental Investigation, Int. J. Solids Struct., 29 (1992) 339-420.

[12] P.M. Cunniff, Dimensionless Parameters for Optimization of Textile Based Body Armor Systems, in: Proceedings of the 18th International Symposium on Ballistics, San Antonio, Texas, 1999, pp. 1303-1310.

[13] K. Karthikeyan, B.P. Russell, N.A. Fleck, H.N.G. Wadley, V.S. Deshpande, The effect of shear strength on the ballistic response of laminated composite plates, Eur. J. Mech. A-Solids, 42 (2013) 35-53.

[14] C. Zener, The intrinsic inelasticity of large plates, Phys. Rev., 59 (1941) 669-673.

[15] R. Olsson, Impact response of orthotropic composite plates predicted from a one-parameter differential equation, AIAA Journal, 30 (1992) 1587-1596.

[16] C.T. Sun, S. Chattopadhyay, Dynamic response of anisotropic laminated plates under initial stress to impact of a mass, J. Appl. Mech., 42 (1975) 693-698.

[17] J.M. Whitney, N.J. Pagano, Shear Deformation in Heterogeneous Anisotropic Plates, J. Appl. Mech., 37 (1970) 1031-1036.

[18] A.L. Dobyns, Analysis of simply-supported orthotropic plates subject to static and dynamic loads, AIAA Journal, 19 (1981) 642-650.

[19] Y. Qian, S.R. Swanson, Experimental measurement of impact response in carbon/epoxy plates, AIAA Journal, 28 (1990) 1069-1074.

[20] M.S. Hoo Fatt, L. Palla, Analytical Modeling of Composite Sandwich Panels under Blast Loads, J. Sandw. Struct. Mater., 11 (2009) 357-380.

[21] S.L. Phoenix, P.K. Porwal, A new membrane model for the ballistic impact response and V_{50} performance of multi-ply fibrous systems, Int. J. Solids Struct., 40 (2003) 6723-6765.

[22] R.L. Sierakowski, S.K. Chaturvedi, Dynamic loading and characterization of fiber-reinforced composites, Wiley-Interscience, New York, USA, 1997.

[23] A. Schiffer, V.L. Tagarielli, The dynamic response of composite plates to underwater blast: theoretical and numerical modelling, Int. J. Impact Eng., 70 (2014) 1-13.

[24] F. Latourte, D. Gregoire, D. Zenkert, X. Wei, H.D. Espinosa, Failure mechanisms in composite panels subjected to underwater impulsive loads, J. Mech. Phys. Solids, 59 (2011) 1623-1646.
[25] N. Takeda, R.L. Sierakowski, L.E. Malvern, Wave propagation experiments on ballistically impacted composite laminates, J Compos Mater, 15 (1981) 157-174.
[26] P.D. Soden, M.J. Hinton, A.S. Kaddour, Lamina properties, lay-up configurations and loading conditions for a range of fibre-reinforced composite laminates, Compos Sci Technol, 58 (1998) 1011-1022.

Tables

Table 1: Elastic properties and tensile failure strains of the CFRP and GFRP laminae considered in this study, as reported in Soden et al. [26].

	E_1 (GPa)	E_2 (GPa)	ν_{12}	ν_{21}	ν_{23} (GPa)	$G_{12} = G_{13}$ (GPa)	G_{23} (GPa)	ε^*_{1T} (%)
CFRP	126	11	0.28	0.024	0.4	2.6	3.9	1.38
GFRP	45.6	16.2	0.28	0.1	0.4	6.6	5.8	2.8

Table 2: Stacking sequences, thicknesses, densities and effective elastic properties (eq. (13)) of selected GFRP and CFRP laminates.

lamina material	layup	h (mm)	ρ (kgm^{-3})	$\tilde{E}_r$ (GPa)	$\tilde{\nu}_{r\varphi}$	$\tilde{G}_r$ (GPa)
CFRP	$[0,45,90,-45]_{2s}$	2.5	1580	51.06	0.29	5.26
CFRP	$[0,90]_{5s}$	2.5	1580	45.6	0.15	5.26
GFRP	$[0,90]_{5s}$	2.5	2030	24.4	0.26	5.81

Figures

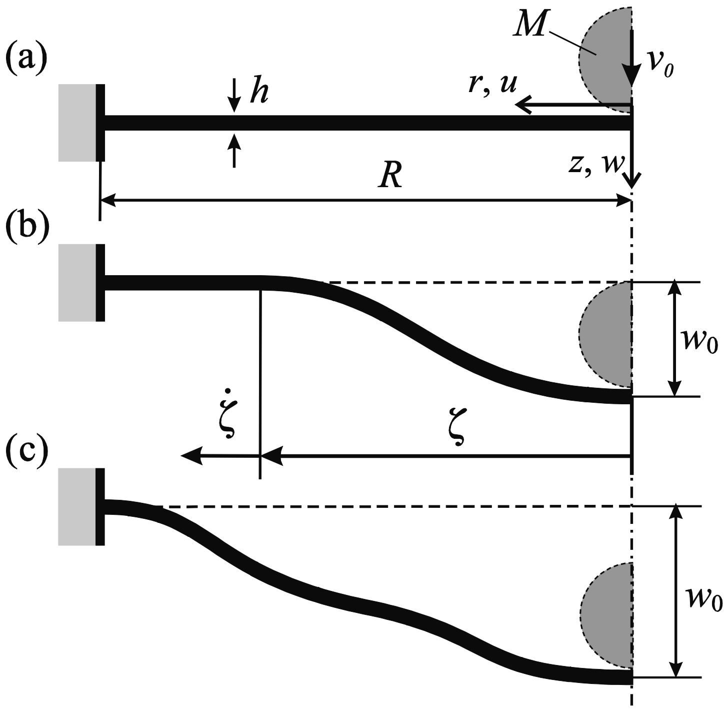

Fig. 1 Sequence of deformation profiles associated with the response of a clamped elastic plate subject to impact of a rigid projectile: (a) projectile impinges on the target, (b) propagation of a flexural wave (Phase 1 response) and (c) excitation of higher order mode shapes due to boundary effects (Phase 2 response).

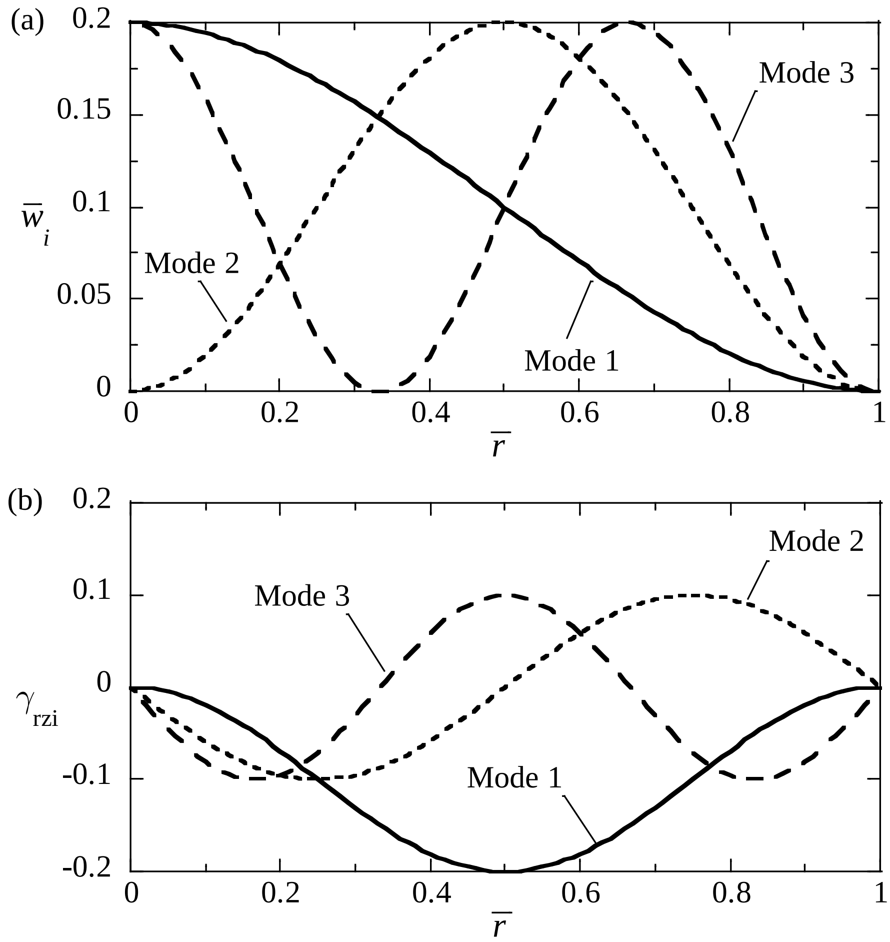

Fig. 2 Various mode shapes used to describe the Phase 2 response of the plate: (a) normalised plate deflection $\overline{w}_i = w_i / R \ \left(i = 0,1,2\right)$, and (b) transverse shear deformation $\gamma_{rzi} \ \left(i = 0,1,2\right)$ as functions of the normalised radius $\overline{r} = r / R$.

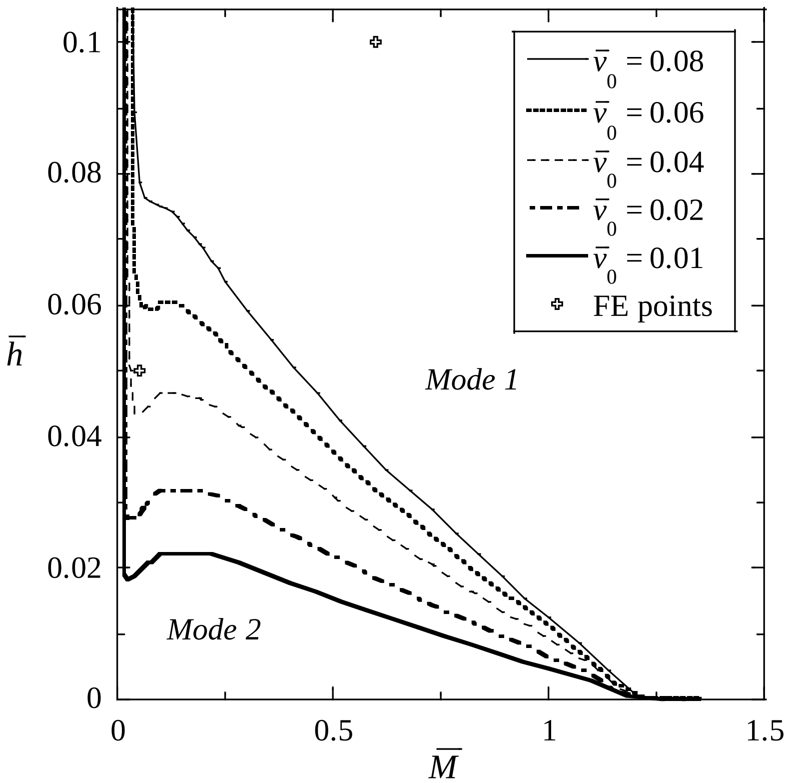

Fig. 3 Non-dimensional chart in the $\bar{M} - \bar{h}$ space showing the transitions between the two characteristic deformation modes for the case of elastic isotropic plates with $\nu = 0.25$ ($\bar{G} = 0.4$); contours of non-dimensional impact velocity $\bar{v}_0$ are included.

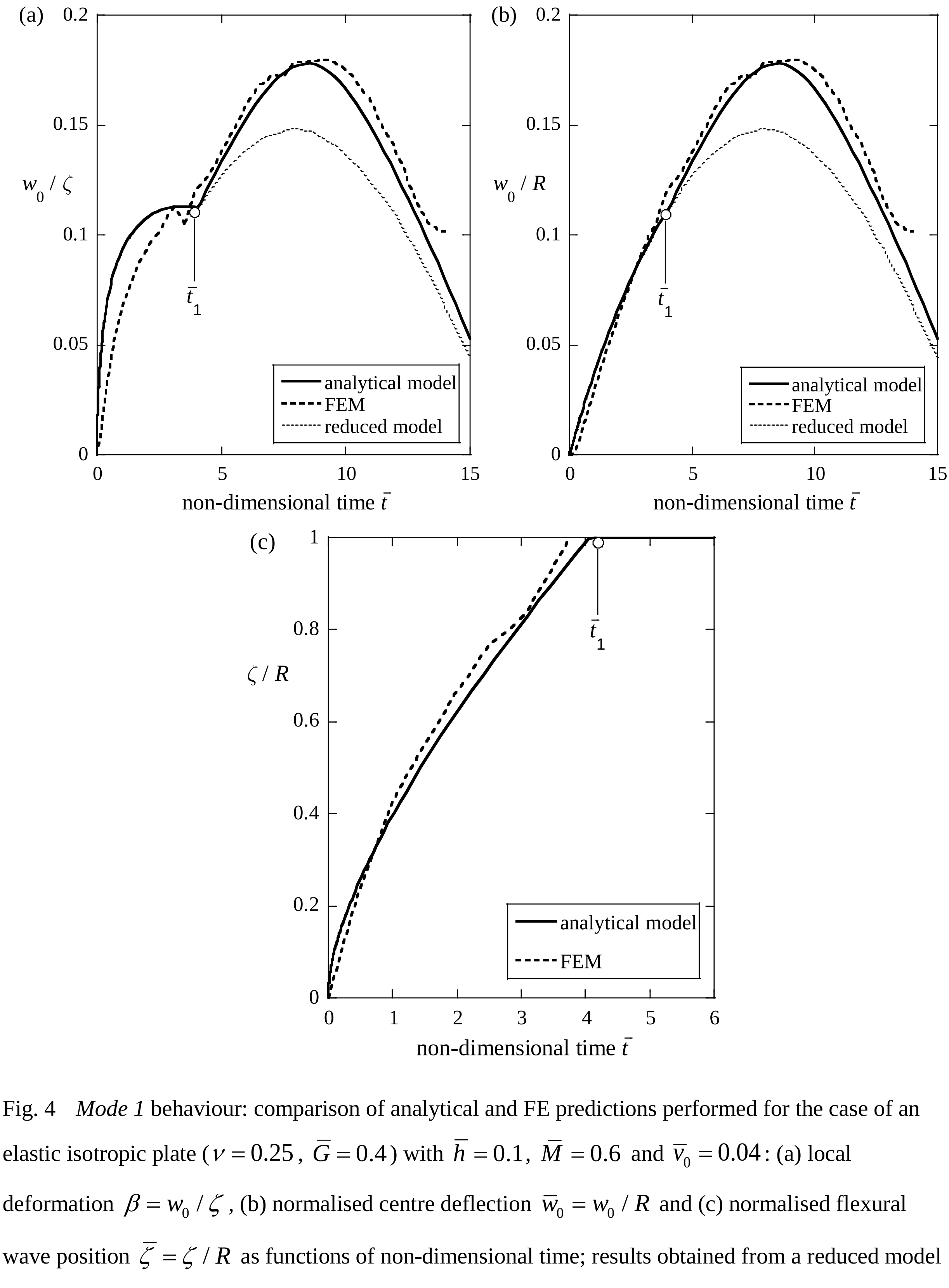

Fig. 4 *Mode 1* behaviour: comparison of analytical and FE predictions performed for the case of an elastic isotropic plate ($\nu = 0.25$, $\bar{G} = 0.4$) with $\bar{h} = 0.1$, $\bar{M} = 0.6$ and $\bar{v}_0 = 0.04$: (a) local deformation $\beta = w_0 / \zeta$, (b) normalised centre deflection $\bar{w}_0 = w_0 / R$ and (c) normalised flexural wave position $\bar{\zeta} = \zeta / R$ as functions of non-dimensional time; results obtained from a reduced model are included in (a) and (b) for comparison.

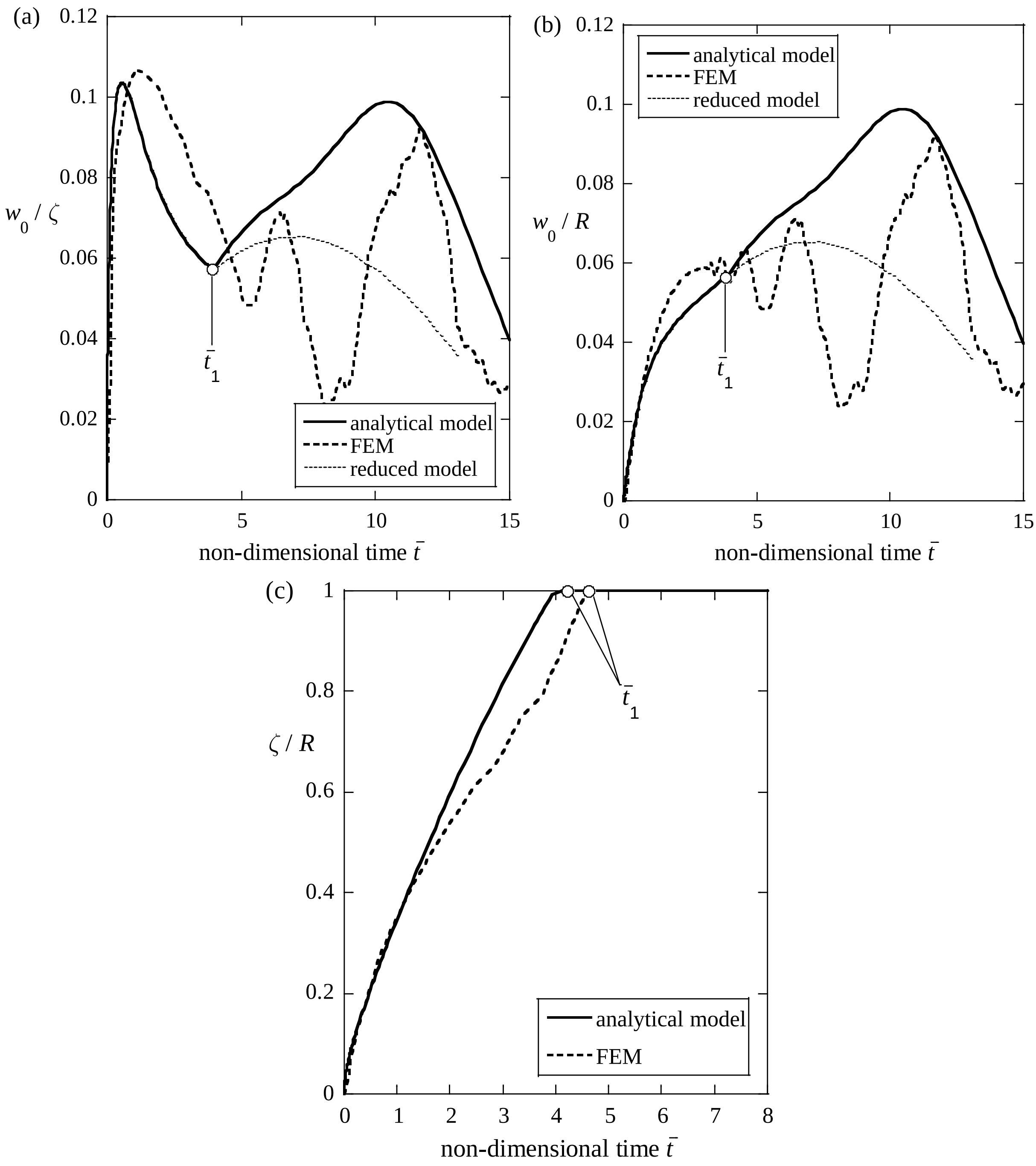

Fig. 5 *Mode 2* behaviour: comparison of analytical and FE predictions performed for the case of an elastic isotropic plate ($\nu = 0.25$, $\bar{G} = 0.4$) with $\bar{h} = 0.05$, $\bar{M} = 0.05$ and $\bar{v}_0 = 0.055$: (a) local deformation $\beta = w_0 / \zeta$, (b) normalised centre deflection $\bar{w}_0 = w_0 / R$ and (c) normalised flexural wave position $\bar{\zeta} = \zeta / R$ as functions of non-dimensional time; results obtained from a reduced model are included in (a) and (b) for comparison.

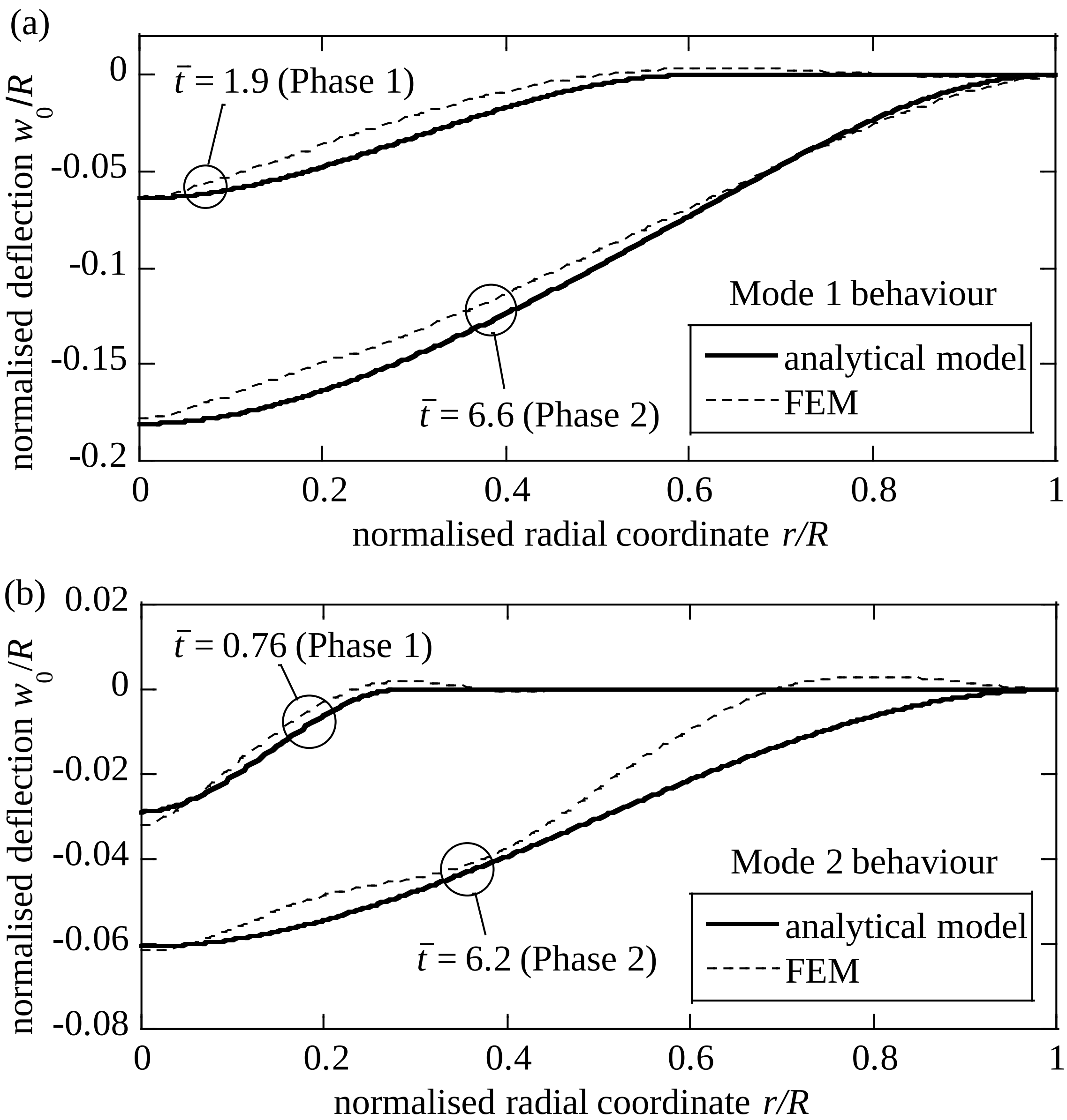

Fig. 6 Snapshots of normalised deflection profiles for elastic isotropic plates ($\nu = 0.25$, $\bar{G} = 0.4$): (a) Mode 1 behaviour with $\bar{h} = 0.1$, $\bar{M} = 0.6$ and $\bar{v}_0 = 0.04$; (b) Mode 2 behaviour with $\bar{h} = 0.05$, $\bar{M} = 0.05$ and $\bar{v}_0 = 0.055$; analytical and FE predictions are compared.

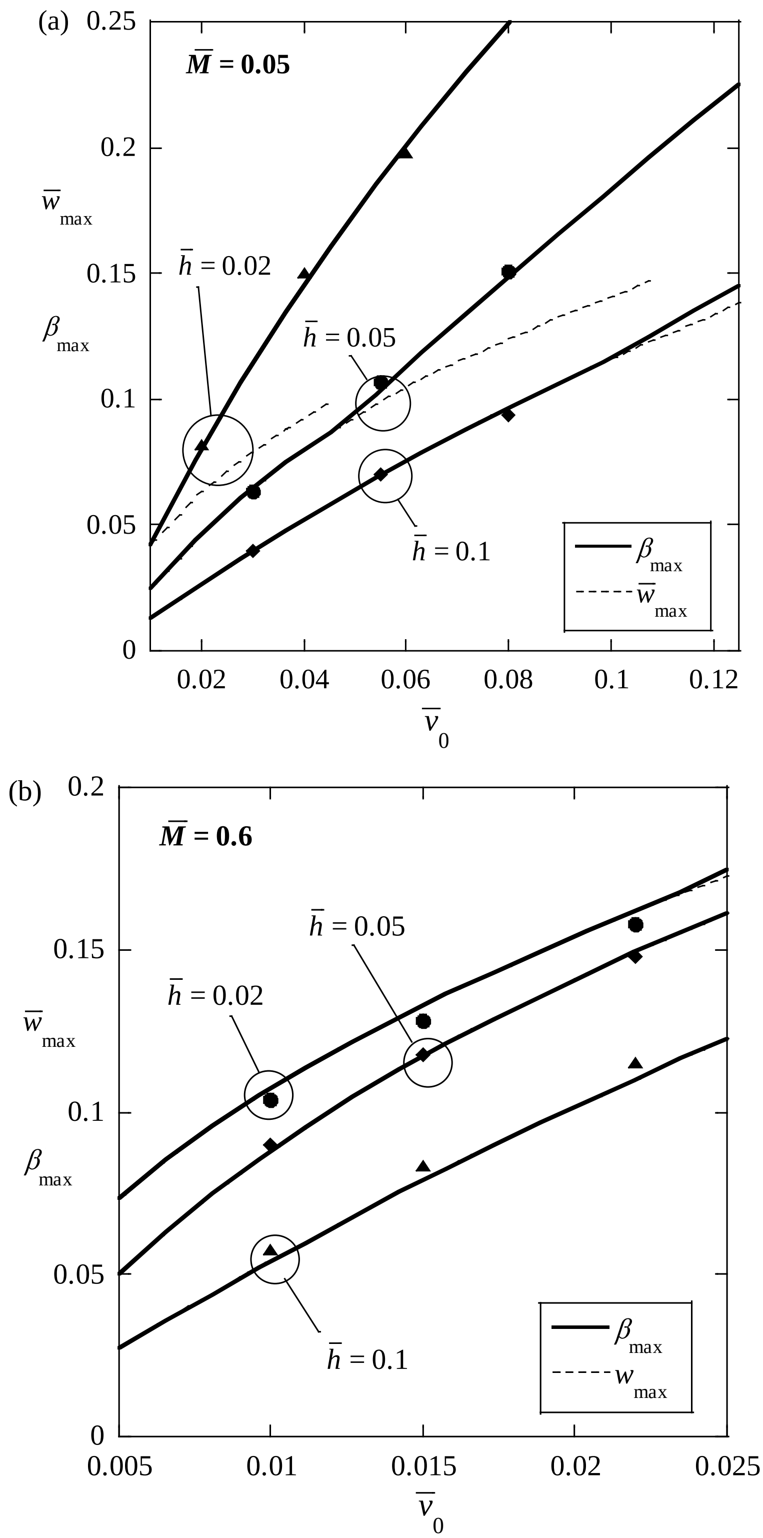

Fig. 7 Analytical predictions of the maximum normalised centre deflection (dashed lines), $\bar{w}_{\max} = \max\left(w_0 / R\right)$, and local deflection (solid lines), $\beta_{\max} = \max\left(w_0 / \zeta\right)$, for the case of elastic isotropic plates ($\nu = 0.25$, $\bar{G} = 0.4$) with $\bar{M} = 0.05$ (a) and $\bar{M} = 0.6$ (b); contours of aspect ratio $\bar{h} = h / R$ are plotted for three different values and FE predictions of $\beta_{\max}$ are included for comparison.

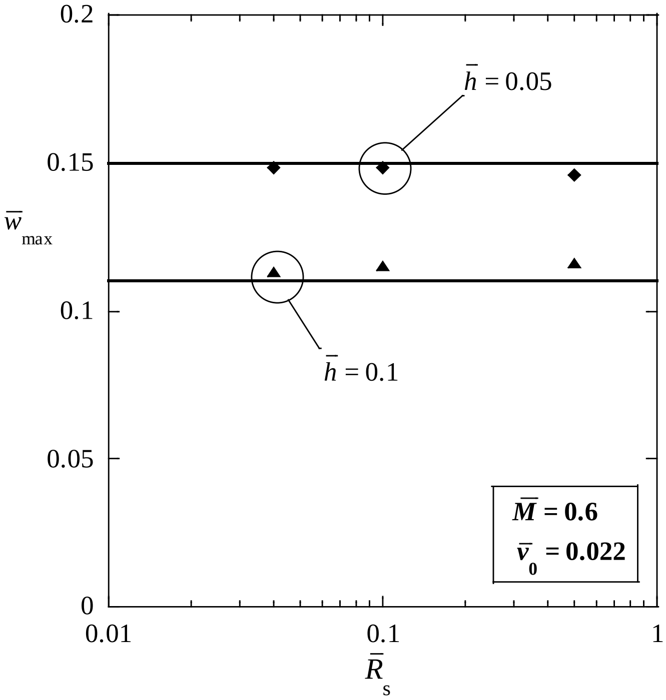

Fig. 8 Analytical and FE predictions of the maximum normalised centre deflection, $\bar{w}_{\max} = \max\left(w_0 / R\right)$, as functions of the normalised projectile radius $\bar{R}_s = R_s / R$ for the choices $\bar{M} = 0.6$ and $\bar{v}_0 = 0.022$; contours of aspect ratio are included for $\bar{h} = 0.05$ and $\bar{h} = 0.1$; the material properties were taken as $E = 50$ GPa and $\nu = 0.25$.

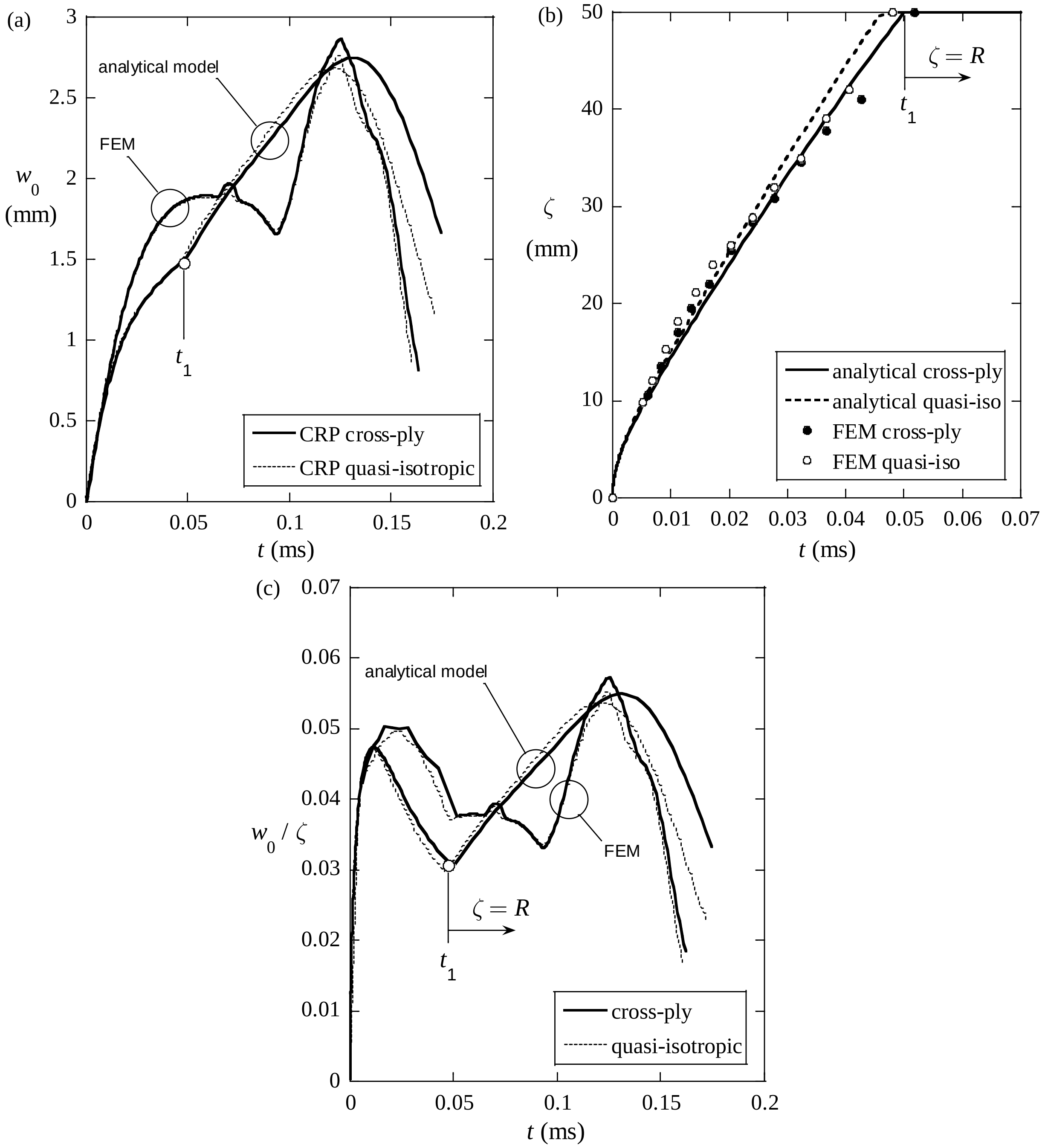

Fig. 9 Analytical and FE predictions of the deformation response for the case of CFRP plates with aspect ratio $\bar{h} = 0.05$ (see Table 2) subject to ballistic impact by a rigid ball projectile of mass $M = 3.1\,\mathrm{g}$ and velocity $v_0 = 86\,\mathrm{ms}^{-1}$; both cross-ply $[0,90]_{5s}$ and quasi-isotropic $[0,45,90,-45]_{2s}$ layups are considered: (a) centre deflection w_0, (b) flexural wave position ζ, and (c) normalised local deformation $\beta = w_0 / \zeta$ as functions of time.

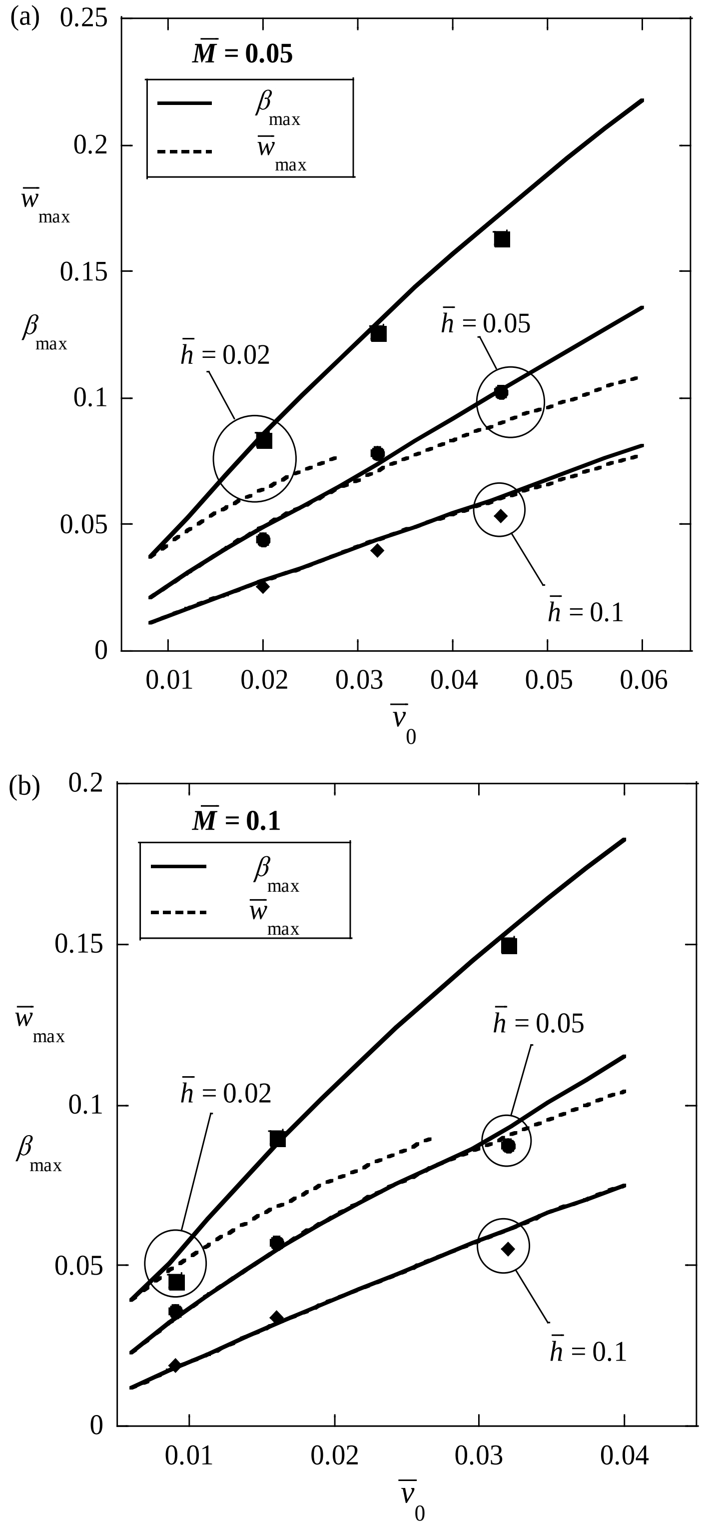

Fig. 10 Analytical predictions of the maximum normalised centre deflection (dashed lines), $\bar{w}_{\max} = \max\left(w_0 / R\right)$, and local deflection (solid lines), $\beta_{\max} = \max\left(w_0 / \zeta\right)$, for the case of cross-ply CFRP plates (stacking sequence $[0,90]_{ns}$, see Table 2) with $\bar{M} = 0.05$ (a) and $\bar{M} = 0.1$ (b); contours of aspect ratio $\bar{h} = h / R$ are plotted for three different values, and FE predictions of $\beta_{\max}$ are included for comparison.

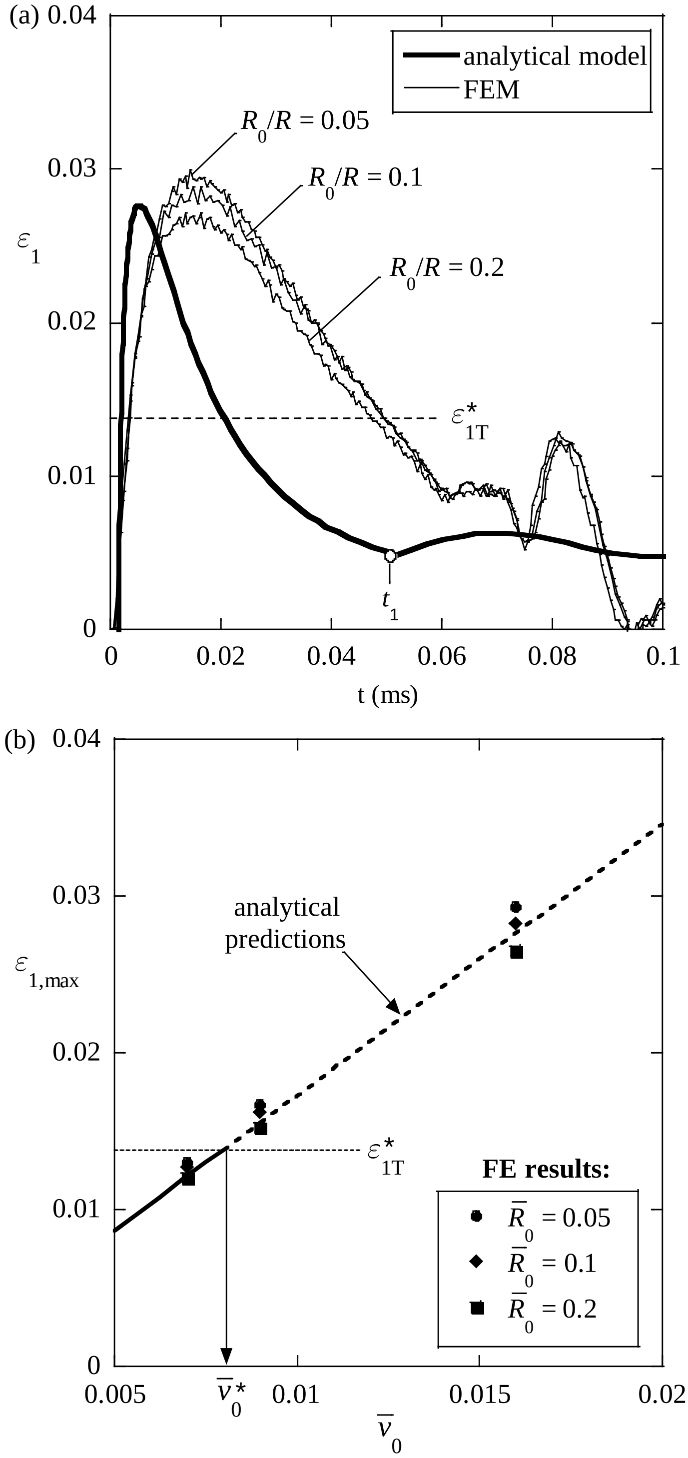

Fig. 11 Analytical and FE predictions of strain induced at the the tensile face of a CFRP plate (stacking sequence $[0,90]_{5S}$, aspect ratio $\bar{h} = 0.05$) below the impact point for the choice $\bar{M} = 0.1$: (a) fibre strain versus time histories, $\varepsilon_1(t)$, for the case $\bar{v}_0 = 0.016$, and (b) sensitivity of the peak tensile fibre strain, $\varepsilon_{1,\max} = \max\left[\varepsilon_1(t)\right]$, to variations of non-dimensional velocity, $\bar{v}_0$.

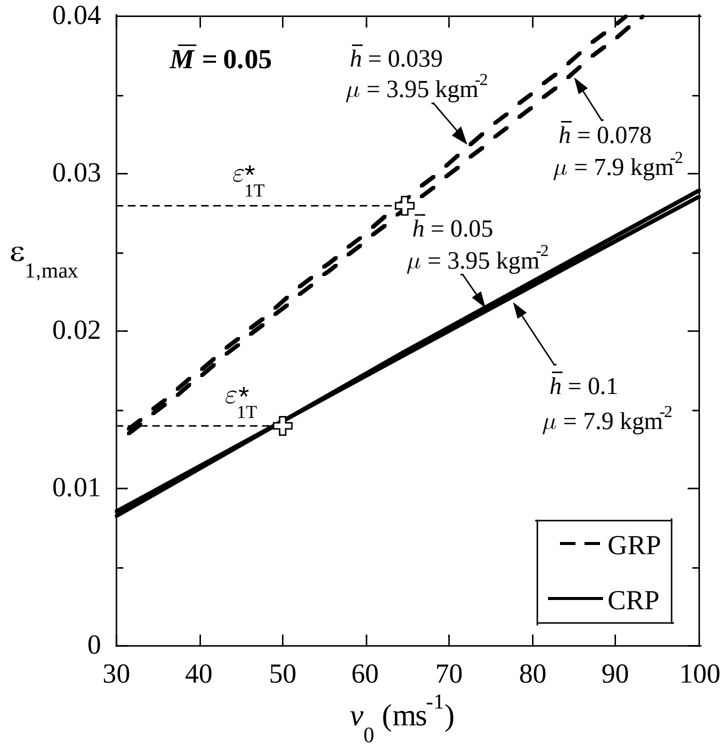

Fig. 12 Analytical predictions of maximum tensile fibre strain, $\varepsilon_{1,\max} = \max\left[\varepsilon_1(t)\right]$, as a function of impact velocity, v_0, for CFRP and GFRP plates with equal mass and layup $[0,90]_{ns}$; contours of aspect ratio $\bar{h} = h/R$ are included for the choice $\bar{M} = 0.05$.

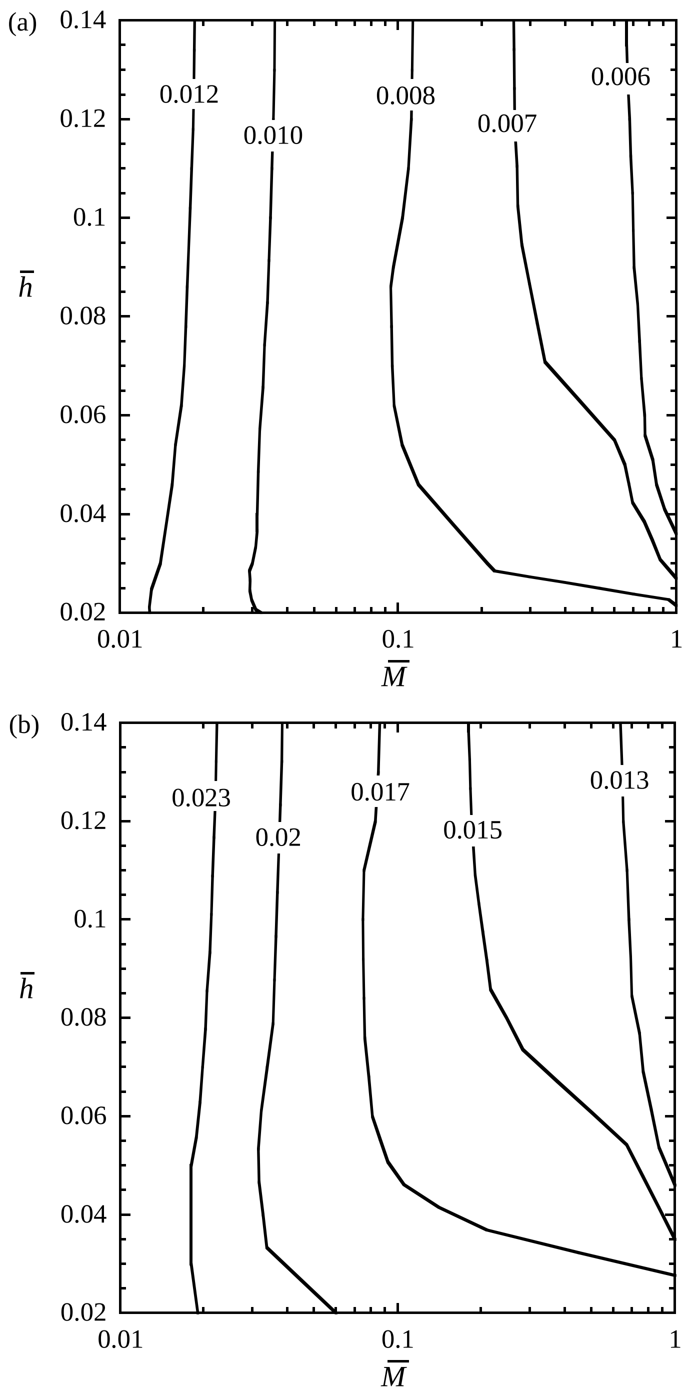

Fig. 13 (a) Design chart in the $\bar{M}-\bar{h}$ space for the case of CFRP laminates ([0,90]$_{ns}$, $\bar{G}=0.12$, $\tilde{v}_{r\varphi}=0.15$, see Table 2) with contours of non-dimensional critical impact velocity, $\bar{v}_0^* = v_0^*\sqrt{\rho/\tilde{E}_r}$, at the onset of tensile failure failure, $\varepsilon_{1,\max}=\varepsilon_{1T}^*=1.38\%$; (b) similar design chart for GFRP laminates ([0,90]$_{ns}$, $\bar{G}=0.24$, $\tilde{v}_{r\varphi}=0.26$, see Table 2) with higher ductility, $\varepsilon_{1T}^*=2.8\%$.